Dynamic Nuclear Polarization

at

High Magnetic Fields in Liquids

C. Griesinger[a]*, M. Bennati*[a]*, H. M. Vieth*[b] *C. Luchinat*[c]*, G. Parigi*[c]*,*

P. Höfer[d]*, F.Engelke*[d]*, S. J. Glaser*[e]*, V. Denysenkov*[f]*, T. F. Prisner***[f]

[a]*MPI for Biophysical Chemistry Göttingen, Am Fassberg 11, 307077 Göttingen, Germany*

[b]*Free University Berlin, Inst. of Experimental Physics, Arnimallee 14, 14195 Berlin, Germany*

[c]*Magnetic Resonance Center (CERM) and Department of Chemistry, University of Florence,*
Via Luigi Sacconi 6, 50019, Sesto Fiorentino, Italy

[d]*Bruker Biospin GmbH, Rheinstetten,*

[e]*Technische Universität München, Department of Chemistry, Lichtenbergstr. 4, 85747*
Garching, Germany

[f]*Goethe University Frankfurt, 60438 Frankfurt, Germany*

**Corresponding author. Tel.: +49 (0) 69 798 29406; fax: +49 (0) 69 7929404*

Email address: Prisner@Chemie.Uni-Frankfurt.de

Keywords: Dynamic nuclear polarization, DNP, Overhauser Effect, High-resolution NMR, High magnetic fields, Hyperpolarization

Highlights:

- High field Dynamic Nuclear Polarization spectrometers for liquid samples have been constructed, working at 7, 9.2 and 14 T, respectively.
- The field dependence of the Overhauser DNP efficiency has been measured experimentally for the first time up to a field of 9.2 T and compared with experimental results from NMRD, MD and theoretical models.
- Coherent and relaxation effects within fast magnetic field changes have been observed and quantitatively analyzed.
- High Overhauser DNP enhancements for liquid samples have been observed at high magnetic field.

Graphical Abstract:

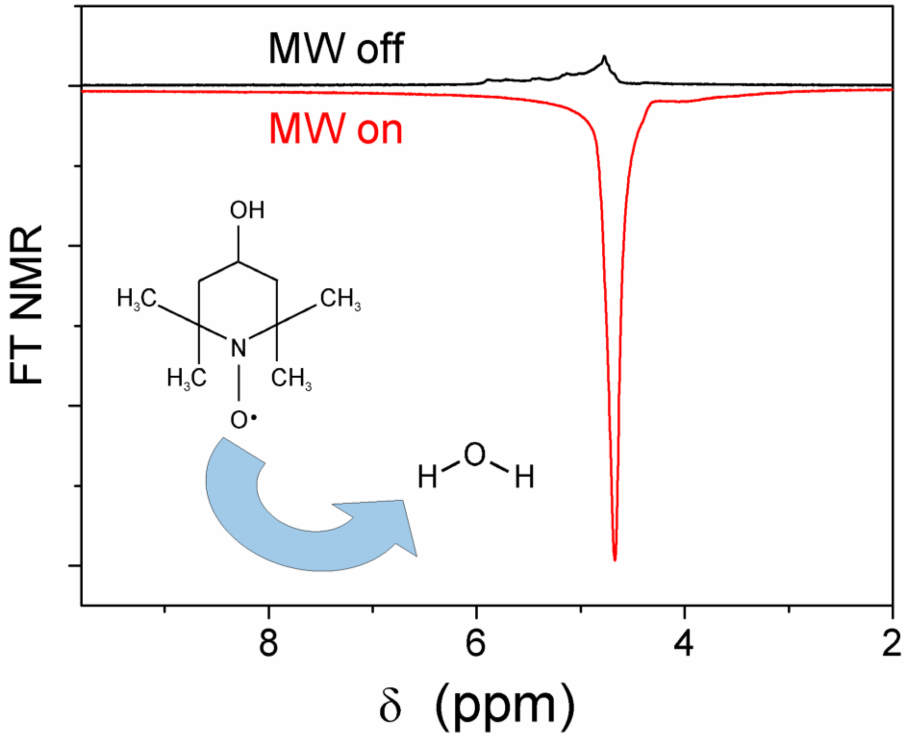

Contents

1. Introduction

NMR is a versatile spectroscopic technique which allows investigating structural and dynamic aspects of macromolecules in their natural surrounding with atomic detail. Its drawback, compared to many other spectroscopic techniques is its intrinsic low sensitivity due to the small energy splitting of nuclear spin states. Therefore improving sensitivity is a key issue in NMR spectroscopy. Several important inventions have boosted the sensitivity of NMR spectroscopy and allowed new application areas to be explored. NMR signal intensity and resolution has been improved by increasing the external magnetic field strength. Further improvements were made using nuclear-nuclear cross-polarization schemes, usually from protons (with a large gyromagnetic ratio) to carbon-13 or nitrogen-15 (with much smaller gyromagnetic ratios, $\gamma_p/\gamma_c \sim 4$ for carbon and $\gamma_p/\ \gamma_n \sim 10$ for nitrogen) **[1]**. Cryogenic cooling of the coil, while keeping the sample at room temperature, additionally improved the sensitivity by a factor of about 3.

Albert W. Overhauser proposed to polarize nuclei in metals by applying microwave excitation to the electron resonance transition **[2]**. The experimental proof of this concept on Li metal at low magnetic fields appeared even before the theoretical paper was published **[3]**. Soon, this concept was extended to polarization transfer from free radicals to solvent molecules **[4]** and numerous applications in liquids were found **[5,6]**. The polarization transfer of the so-called 'Overhauser Effect' is mediated via relaxation mechanisms, introduced by the time dependent fluctuations of the scalar and dipolar coupling between electron and nuclear spins.

In solids such spin-spin relaxation processes are ineffective, but it was recognized by Jeffries **[7]** and Abragam **[8]** that, instead, forbidden electron-nuclear spin transition in solids can be used to achieve nuclear polarization. More elaborate mechanisms for polarization transfer from electron to nuclear spin involving more than two spins were found in solids, called the 'Cross Effect', **[9-12]** and 'Thermal Mixing' **[13-15]**.

Dynamic nuclear polarization (DNP) refers to all these mechanisms which transfer electron spin polarization to nuclear spins by resonant microwave excitation of electron spin transitions. The maximum DNP enhancement of the NMR signal is given by the electron to nuclear gyromagnetic ratios γ_e/γ_n, which for proton spins is a factor of 660. Therefore, DNP has the potential to strongly increase the sensitivity of NMR, much beyond nuclear-nuclear cross-polarization schemes. Unfortunately, all these DNP mechanisms rapidly become inefficient at higher magnetic fields and decrease with B_0^{-2}. Thus with the development of high-field NMR spectrometers, DNP was not considered to be useful at higher magnetic fields and only few solid-state DNP applications at magnetic fields higher than 1 T were reported **[16-18]**.

The situation changed drastically for NMR applications in solids by the pioneering work of the Griffin group at MIT, who succeeded to obtain substantial DNP enhancements in solids at high magnetic fields (5 T). Enhancements at the theoretical limit (400±50) have been reached with TEMPO nitroxide radicals and only 17 mW of microwave power at 12 K, utilizing a microwave resonant cavity **[19]**. DNP enhancements as large as 300 could be obtained under magic-angle sample spinning (MAS) conditions at 90 K **[20]**, using biradicals as DNP agents **[21]** and a high power gyrotron microwave source **[22]** at 140 GHz frequency.

For liquid state NMR spectroscopy the Amersham Health Research Laboratory in Sweden used a new approach where a pellet sample, containing trityl radicals at high concentration, is polarized at very low temperatures (1.6 K) and high magnetic field (3.4 T). After the polarization process at low temperatures, the sample is dissolved and diluted with hot solvent within a few seconds and transferred to the NMR magnet for detection. This allowed obtaining highly polarized carbon-13 and nitrogen-15 nuclei with effective enhancements above 10000 **[23, 24]**. The drawback of this very impressive experiment is that the sample has to be frozen and can only be used once after the melting or dissolution process; furthermore, the polarization process takes about one hour or more. Based on this encouraging high field

DNP results obtained in solids, we started a collaborative research project in the framework of an EU-Design study (Bio-DNP) to explore the potential of DNP for high-resolution NMR applications at high magnetic fields where the sample is kept in the liquid state. A major goal was to experimentally explore the field dependence of the Overhauser DNP enhancement beyond the formerly reached 1.25 T **[25]** to higher magnetic field values (up to 9.4 T). Two different experimental approaches were exploited: (1) polarization transfer at low magnetic fields with a subsequent fast shuttle of the liquid sample or alternatively, the whole NMR probe to the high NMR field (referred to as Shuttle-DNP) and (2) microwave excitation directly at the NMR detection field (called High-Field-DNP).

In the following sections, after briefly reviewing the theoretical background of DNP in liquids, first the main features of the home-built high-field liquid DNP setups, which are the basis of the new experimental results, will be described in detail as well as some other methods used to extract important parameters describing the coupled spin-system. Afterwards the experimental results on nitroxide radicals in water, used as a specific DNP agent/target system, will be discussed. Electron spin saturation, electron and nuclear relaxation rates, and DNP enhancements have been obtained over a very wide magnetic field range (0-10 T). Additionally, coherent effects on the hyperpolarized spin system within a shuttle process from low to high magnetic field have been investigated and strategies to increase the DNP enhancement with pulse microwave excitation or optimum control excitation sequences were studied. Finally, we will conclude by comparing our results with theoretical models and predict, based on these results, optimal DNP performances at high magnetic fields for liquid samples.

2. Theoretical Background

2.1.Overhauser Enhancement in Liquids

Extensive reviews on the theoretical models describing the Overhauser effect for liquid samples can be found in the literature **[5, 6]**; therefore only a very brief description will be summarized herein. All theoretical descriptions of Overhauser DNP in liquids are based on the Solomon equation **[26]**:

$$\frac{dI_z}{dt} = -\left(\rho_I + W^0\right)\left(I_z - I_0\right) - \sigma_{IS}\left(S_z - S_0\right) \tag{1}$$

where I and S refer to the nuclear and electron spin, respectively, I_0 and S_0 being their Boltzmann equilibrium values. The relaxation rates ρ_I and σ_{IS} are given by the nuclear-electron zero-, one- and two-quantum transitions and are defined by $\rho_I = W_0 + 2W_I + W_2$ and $\sigma_{IS} = W_2 - W_0$. All the transitions with their respective rates W are illustrated in the energy level diagram of Figure 1. The steady-state solution of equation (1) under continuous microwave irradiation of the allowed electron spin transition leads to the well known Overhauser enhancement formula **[5]**:

$$\varepsilon = \frac{I_z - I_0}{I_0} = -\xi f s \frac{\gamma_e}{\gamma_n} \tag{2}$$

The enhancement ε of the nuclear spin polarization is given by the ratio of the gyromagnetic ratios of electron and nuclear spin multiplied by the coupling factor ξ, the leakage factor f and the saturation factor s.

The coupling factor ξ describes the efficiency of the cross-relaxation processes and is given by:

$$\xi = \frac{\sigma_{IS}}{\rho_I} = \frac{W_2 - W_0}{W_0 + 2W_I + W_2}\,. \tag{3}$$

The leakage factor f accounts for the nuclear spin relaxation from the electron spin compared to other mechanisms:

$$f = \frac{\rho_I}{\rho_I + W^0} = \frac{W_0 + 2W_I + W_2}{W_0 + 2W_I + W_2 + W^0} = 1 - \frac{T_{1I}}{T_{1I}^0}\,, \tag{4}$$

where T_{1I} and T^0_{1I} are the longitudinal nuclear relaxation times in the presence and absence of paramagnetic species, respectively. W^0 is the nuclear spin relaxation rate resulting from all processes not related to the nuclear-electron spin interaction.

Finally, the saturation factor s describes the efficiency of the microwave pumping. For a single homogeneous EPR line, s can easily be derived from the Bloch equations **[27]**:

$$s = \frac{S_0 - \langle S_z \rangle}{S_0} = \frac{\gamma_e^2 B_1^2 T_{1S} T_{2S}}{1 + \gamma_e^2 B_1^2 T_{1S} T_{2S}}, \tag{5}$$

where B_1 is the magnetic field strength of the microwave in the rotating frame and T_{1S} and T_{2S} are longitudinal and transversal relaxation times of the electron spin, respectively.

2.2. Determination of Leakage, Saturation and Coupling Factor

The leakage factor can be easily accessed experimentally by measuring the nuclear spin longitudinal relaxation time in the presence and absence of paramagnetic molecules, as can be inferred from Eq. (4). For concentrations of paramagnetic molecules in the mM range, which are typically used for DNP applications, this factor will tend to 1. The saturation factor s also ranges from 0 to 1 and can in principle be determined from EPR saturation experiments. Unfortunately, for commonly used nitroxide radicals in solution, the transversal relaxation times are in the low ns regime at room temperature and high magnetic fields. Furthermore, saturating the EPR lines requires large MW power, which - depending on the solvent – can lead to excessive sample heating. Especially for nitroxide radicals the situation is even more complicated, because the EPR spectrum consists of two (for ^{15}N) or three hyperfine lines (for ^{14}N), separated by up to 100 MHz in frequency. Thus, not all hyperfine lines can be excited simultaneously by the microwave B_1 field strengths achievable. In this case, partial saturation of the non-excited hyperfine lines is achieved by Heisenberg spin exchange at the high radical concentrations used for the DNP experiments. Such effects have been theoretically analyzed and experimentally observed by EPR and ELDOR (electron-electron double resonance) experiments **[28-33]**. For transition metal ions the relaxation rates are much higher, rendering

EPR detection at room temperature extremely demanding. NMR relaxation measurements can be used to estimate the electron spin relaxation rates **[34]** and, based on that, the achievable electron spin saturation.

The DNP enhancement ε increases linearly with microwave power, for low microwave power far away from saturation (s<<1) and a single homogeneous line, as can be seen from Eq. (5). Therefore, a plot of $1/\varepsilon$ as a function of $1/P_{mw}$ (see Figure 13 below) can be utilized to estimate the maximum enhancement for full saturation ε_{max} and from the latter the coupling factor ξ can also be obtained, without having to explicitly determine the saturation factor.

The coupling factor ξ depends on the dynamics and the energetics of the electron-nuclear spin system. For pure dipolar coupling it is a positive quantity, which can take the maximum value of 0.5 at low magnetic field values and decreases with increasing magnetic field. The field dependence of this factor is mainly responsible for the reduced Overhauser DNP efficiency at higher magnetic fields (Figure 2). It depends on the magnitude of 'forbidden' zero- and double-quantum relaxation rates compared to the 'allowed' single-quantum relaxation rates (see Equation 3). For an electron-nuclear spin system the zero- and double-quantum transitions at frequencies $\omega_{DQ/ZQ}=\omega_S \pm \omega_I$ are both very close to the electron Larmor frequency ω_S. At high magnetic fields both cross-relaxation rates are very low, leading to a small coupling factor and thus small DNP efficiency. At a magnetic field of 9.4 T the electron spin resonance frequency corresponds to ν_S=260 GHz and the nuclear resonance frequency for a proton spin to ν_I = 400 MHz. The spectral density function is described by a Lorentzian function $J(\omega,\tau_c)=\dfrac{\tau_c}{1+\omega^2\tau_c{}^2}$ for stochastic processes with an exponential autocorrelation function and a characteristic correlation time constant τ_c. Therefore stochastic processes modulating the electron-spin interaction with a correlation time $\tau_c > 1/\omega_S$, corresponding to 0.6 ps at 260 GHz electron Larmor frequency, will contribute less and less to the cross-relaxation rates and thus also to the coupling factor and the DNP enhancement **[35]**. The frequency dependence of the stochastic processes responsible for cross-relaxation therefore determines the field dependence of the Overhauser DNP effect for electron-nuclear spin systems. If electron-nuclear scalar coupling is active, for example for nuclei spins of the radical itself, $\xi = -1$, independent of magnetic field. Therefore, if both scalar and dipolar coupling are present, ξ can range from -1 to +0.5. Intermolecular polarization transfer from a radical (with spin S) to a diamagnetic target molecule (with spin I) is dominated by the dipolar hyperfine coupling modulated by the translational or rotational diffusion of both molecules. In this case, the coupling factor is approximately given by **[36]**:

$$\xi_{dip} = \frac{5J(\omega_s,\tau)}{7J(\omega_s,\tau)+3J(\omega_I,\tau)} \quad . \tag{6}$$

If $\omega_S\tau \ll 1$ this results in a coupling factor of 0.5 and a DNP enhancement of -330. On the other hand, if $\omega_S\tau > 1$ and $\omega_I\tau < 1$ the coupling factor will decrease with ω_S^{-2}, or equivalently, quadratic with the magnetic field B_0 (Figure 2). At high magnetic fields the translational motion will be the dominant contribution to the coupling factor and the resulting DNP effect. For a simple force-free model of freely diffusing molecules, which assumes the interacting spins to be at the centers of spherical molecules, the translational correlation time τ_t is related to the diffusion coefficients of the radical (D_S) and the target molecule (D_I) and the distance of closest approach between them ($d=r_s+r_I$) by **[37]**:

$$\tau_t = \frac{d^2}{D_S + D_I} \tag{7}$$

with r_S and r_I being the molecular radius of radical and target molecule, respectively. Typically, at high magnetic fields the translational correlation time τ_t will be very short compared to T_{1S} but long compared to the inverse electron Larmor frequency ω_S. The spectral density J_t can be calculated to **[38]**:

$$\mathrm{J}_t(z) = \frac{8+5z+z^2}{81+81z+81/2z^2+27/2z^3+4z^4+z^5+z^6/8} \tag{8}$$

with $z = (2\omega\tau_t)^{1/2}$. As a consequence, the coupling factor will decay with $B_0^{\ -3/2}$, if $\omega_S\tau_t > 1$ and $\omega_I\tau_t < 1$.

More advanced models have been developed in order to take into account collisions of radical and target molecules in a more realistic manner **[38]**. Yet, all of them predict very small DNP enhancements in liquids at magnetic field strengths above 5 T. Therefore, when NMR moved to higher magnetic field values, this mechanism was not considered as an option for signal enhancement anymore.

3. Instrumentation

Two experimental setups have been developed to explore the potential of Overhauser DNP at high magnetic fields:

- a *Shuttle-DNP* spectrometer, which excites the electron spin at low magnetic field values (where the DNP efficiency is high) and afterwards shuttles the sample or the whole probe rapidly to a high magnetic field for NMR detection, and
- a *High-Field DNP* spectrometer, which performs the microwave excitation and NMR detection simultaneously at the same magnetic field values.

DNP experiments were carried out at magnetic fields ranging from 0.01 to 10 T to explore the magnetic field dependence of the Overhauser DNP enhancement. NMR relaxation dispersion experiments were conducted from 0 to 24 T magnetic field strength. EPR experiments were performed at X-band (9.5 GHz / 0.34T), Q-band (34 GHz / 1 T), W-band (95 GHz, 3.4 T) and G-band (180 GHz / 6.4 T) microwave frequencies to characterize the electron spin parameters of the paramagnetic molecules used as polarizing agents. In the following the main features and characteristics of the three liquid-DNP spectrometers in Berlin, Frankfurt and Göttingen will be described in more details.

3.1 Shuttle-DNP Spectrometers

The approach of shuttling the sample or the whole NMR probe is based on the fact that polarization transfer processes in liquids can be more efficient and technically less demanding at magnetic field values below 1 T **[5, 6]**. This principle was already exploited by a liquid sample flow system at lower detection fields for applications in analytical chemistry **[39]** and MRI **[40, 41]**. Here, the liquid sample resides inside a microwave cavity for the polarization transfer step. Thus, high microwave magnetic field strengths at the sample are achieved and microwave heating is minimized. This is required to saturate the electron spin system of the radicals due to very short relaxation times in liquid solution at room temperature. Following the polarization process, taking only a few seconds (due to the T_1 relaxation time of the nuclear spins), the sample is physically shuttled to the high magnetic field for NMR detection in a short period of time **[42, 43]**. Alternatively, a rapid transfer of the whole DNP probe was realized **[44]**. Typical transfer times are in the order of a few 10 ms to several 100 ms, depending on the setup and experimental conditions. Shuttling the sample allows very short transfer times of 40 ms in the most recent setup **[43]**. Because the polarization is spatially transferred from a rather low magnetic field to a high NMR detection field, a 'Boltzmann penalty', given by the ratio of the DNP polarization magnetic field (0.3 T or lower) over the NMR detection magnetic field (2 to 14 T), has to be taken into account to calculate the effective DNP enhancement. Another challenge related to this approach concerns coherent and relaxation effects of the coupled spin systems during the transfer from the DNP polarization field to the NMR detection field. The probe shuttle design allowed investigating such effects in great detail. Special care has to be taken to avoid passage through very low magnetic fields, which would result in loss of polarization **[44, 45]**. In the following the shuttle DNP spectrometer (polarizing at a magnetic field of 0.34 T / 9.5 GHz microwave frequency and detecting at a magnetic field of 14 T / 600 MHz proton frequency) built in Göttingen in collaboration with Bruker and the probe shuttle CIDNP/DNP setup developed at the FU Berlin, with MW excitation at several very low magnetic field values (< 0.1T) and detection at 7 T magnetic field, will be described in more detail:

3.1.1. Spectrometer with Pneumatic Sample Shuttle (Göttingen)

The sample shuttle DNP spectrometer (built by Bruker Biospin in collaboration with the MPI for Biophysical Chemistry) consists of a NMR cryomagnet exhibiting a second homogeneous magnetic field region allowing a fast shuttle between pump and detection position. The second homogeneous field spot, located 468 mm above the NMR 'sweet spot' of the magnet, is generated by a ferroshim tube system inserted into the upper magnet bore instead of the standard upper part of the shim tube (Figure 3). The ferroshim system is equipped with additional B_0 correction coils and first-order static gradient coils that allow fine adjustment of the position and the value of the field strength **[43]**. The advantages are:

- a reduction of the distance between the upper position of the shuttling sample, where the DNP is accomplished (0.34 T, 9.5 GHz) and the lower position for NMR detection (14 T, 600 MHz proton NMR frequency), and
- circumventing low field passage effects, which occur in the case that an external, second magnet for the EPR excitation is used **[45, 46]**.

The DNP enhancement at the low field position was optimized by monitoring the water proton NMR signal with a Bruker Minispec spectrometer (^{1}H NMR frequency of 14.5 MHz) and a tuned radio frequency (RF) circuit. A CW MW amplifier (Varian) was used to achieve up to 20 W of pumping power. Radicals, for example perdeuterated TEMPONE-^{15}N, dissolved in water with concentrations of 5-50 mM were loaded into 0.7 to 1 mm inner diameter quartz capillaries to a height of 12 mm (active volume ca. 6 μl) and sealed with plugs made of UV sensitive glue (Vitralit). The quartz capillaries were terminated with toroidal gaskets made of a fluoropolymer on both sides covered by Vespel caps and placed in the shuttle container. At the low field position, the samples were irradiated continuously for variable times between 1 and 20 s and then pneumatically transferred to the high field position, where a 90° pulse was applied to record the NMR spectrum. The overall scheme of the setup and timing is depicted in Figure 4.

Positioned at the low-field plateau position, a cylindrical microwave cavity operating at 9.5 GHz in the TM_{110} mode was installed, equipped with an additional internal Helmholtz coil for NMR detection (Figure 5).

One property of this specific microwave mode is the polarization of the microwave magnetic field along the cavity axis in the transverse direction, at positions where the electric field is zero. Due to the inner diameter of the ferroshim system (40 mm), the maximum possible inner cavity diameter was 32 mm. For the TM_{110} mode this results in a resonance frequency for the empty cavity of f_r = 11.1 GHz. In order to lower the resonance frequency, a PTFE ring was placed inside the cavity to obtain the desired EPR frequency. It was set to a fixed value by variation of the inner and outer diameters of the dielectric ring. A standard UT141 coaxial cable with a short stub for coupling was utilized to couple the cavity to the source. Critical coupling was achieved by altering the penetration depth of the stub into the cavity volume via external mechanics. A typical sample container consisted of a quartz tube with a cylindrical sample diameter of 1 mm and 12 mm axial length (corresponding to an active volume of 6 µl). The shuttle container entered the cavity inside a quartz shuttle tube that is oriented coaxially with respect to the cavity axis. A Helmholtz coil with an axial length of 13 mm has been placed around the shuttle tube. Tuning was realized by external circuit components. In addition to the B_1 and B_2 fields, a modulation field along the direction of the static magnetic field has been applied by a pair of Helmholtz coils above and below the top and bottom plates, each with 100 turns and an inner diameter of 25 mm. In order to allow the modulation field to enter the cavity volume, the top and bottom plates were made from Vespel (Dupont) covered with a thin sheet of copper (thickness ca. 100 µm). The resonance frequency of the cavity (without the Helmholtz coil) could be calculated by the RMM (Radial Mode Matching) technique, suitable to calculate the dimensions of the PTFE ring. Moreover, the drop in cavity Q caused by the dielectric losses in the sample and the dielectric materials could be predicted. For the PTFE material a relative permittivity of 2.08 and a loss tangent of $\tan\delta = 0.0004$ at 9.4 GHz has been assumed. Taking into account a sample diameter of 0.5 mm, a shuttle container of 3.5 mm (outer diameter), and a very low-loss quartz ($\varepsilon_r = 3.78$) shuttle guide of 5 mm (outer diameter), dimensions of 18.9 mm and 26.9 mm for the inner and outer diameter of the PTFE ring, respectively, with an axial cavity length of 30 mm could be estimated. For this setup the calculated overall cavity Q factor was $Q = 1725$. It is worthwhile to note that the RMM technique can only be applied when the cylindrical geometry is maintained. As illustrated in Figure 5, the simulated microwave (electric and magnetic) field distribution in a plane transverse to the resonator axis exhibits the maximum for the magnetic field magnitude and the minimum of the electric field magnitude in the center of the resonator at the sample position.

[Insert Table 1 here]

3.1.2. Spectrometer with Mechanic Probe Shuttle (Berlin)

A different approach was followed at the FU Berlin and is based on the idea to shuttle the whole NMR probe, instead of just the sample. Probe shuttling is performed by a computer-controlled step motor giving rise to a well-defined variation of the time profile of the field variation. Therefore the polarization transfer and relaxation phenomena of hyperpolarized spin systems during the shuttling process may be quantitatively investigated. The probehead was made out of newly developed material, which is light and has zero magnetic susceptibility, thus suppressing the shift of the NMR lines caused by the shuttling process, which otherwise strongly distorts the detected NMR spectra. In addition, the frequency shifts due to eddy currents, being present in conducting parts of the NMR probe because of fast field variation in the field-cycling experiments, have been minimized. As a result the speed of the shuttling could be improved to only 0.27 s from the lowest position (fields below 0.1T) to the detection field of the NMR spectrometer. The probe can be positioned at magnetic fields between 0.05 mT to 7 T, with 0.1 mT resolution in the low field range either in the fringe field of the NMR cryomagnet or in the additional field of an external pair of Helmholtz coils or solenoid (Figure 6). An additional compensation coil has been designed to shield the field of the electromagnet from the position where the NMR spectrum is detected. For multi-scan measurements an external ^{2}H lock for the shuttle spectrometer was implemented. The field gradients are minimized at the low-field region (below 0.1 T), so that the field variation over the sample volume does not exceed 0.01 mT. The mechanical field cycling setup allows us to detect high resolution NMR spectra with a line width below 0.3 Hz under permanent slow sample rotation (0–150 Hz) at B_0=7 T.

This probe field-shuttling spectrometer can measure the nuclear spin relaxation over the whole accessible field range, which covers more than 5 decades of magnetic field strength. A unique feature of this setup is that the fast field-cycling relaxometry can be performed with atomic spectral resolution, i.e., for all spins with different chemical shift individually. This is due to the fact that the field shuttling process was optimized for not affecting the NMR field homogeneity. This spectrometer allows measuring not only DNP but also NMR dispersion, as well as photo- (CINP) or para-hydrogen (PIP) generated hyperpolarization over the whole accessible field range. The probe is equipped with a flexible light-guide and a quartz rod to photo-excite molecules with laser light.

The field-cycling measurement of the microwave-induced DNP enhancements consists of three consecutive steps (Figure 7a). At first, irradiation of the EPR transitions of a stable radical is performed at low field B_{pol} during time $\tau_{irr} \geq 5T_1^n$. This guarantees saturation of the

DNP effect for the nuclear spins. For DNP experiments at variable magnetic fields it is necessary to adjust the EPR frequency to assure pumping at resonance. For comparison, pumping of the EPR transitions has been performed at two different frequencies ν_{irr} (300 MHz and 1.4 GHz). The polarization field B_{pol} was chosen to have ν_{irr} in resonance with one of the electron spin transitions (10 mT for ν_{irr} =300 MHz and 49 mT for ν_{irr} =1.4 GHz). Following irradiation at low field the magnetic field is rapidly changed from B_{pol} to the detection field B_0. Field variation was performed by mechanical shuttling of the whole NMR probe in the fringe field of the 7 Tesla superconducting magnet of our custom-built NMR spectrometer. The total time of the field variation τ_{fv} was 270 ms. Thus, $\tau_{fv} < \frac{1}{3} T_1^n$ and polarization losses during the field variation step are less than 30 %. After the sample arrives at the observation field B_0 the RF-pulse for FID detection is applied and the Fourier transform NMR spectrum is recorded with high spectral resolution.

The pulse sequence used for pumping the EPR transition is shown in Figure 7b. A periodic train of pulses was applied. The duration of each pulse, τ_p, was varied from 5 ns up to 25 μs to change the flip angle, φ, of the electronic magnetization over several periods. Assuming that the high field approximation is sufficiently precise at the low B_{pol} we used standard Bloch equations, i.e., a flip angle $\varphi = \gamma_e B_1 \tau_p$ where B_1 is the amplitude of the co-rotating field component. The RF pulse shape was checked via a pickup antenna positioned near the RF coil and monitored by a digital oscilloscope. For 300 MHz electron spin irradiation frequency, B_1 of the pumping was calibrated by measuring the length of a π/2 pulse for protons at B_0=7 T. In all cases we used relatively short times τ_p in order to minimize effects by the electronic longitudinal and transverse relaxation times, T_1^e and T_2^e respectively.

For DNP experiments at variable magnetic fields it is necessary to combine the field-cycling NMR and EPR pumping. Figure 8 shows the block diagram of the corresponding experiment, where pumping was performed at three frequencies: 75 MHz, 300 MHz and 1.4 GHz. Since the basic design applies to all three cases, we will first describe the 300 MHz variant and, as a supplement, add several minor changes for 1.4 GHz. The 75 MHz variant is broadband and can be tuned between 40 and 100 MHz. Except for the tank circuitry with two orthogonally oriented saddle coils (one tuned to 75 MHz for pumping and the other one to 300 MHz for observation), it is identical with the 300 MHz variant. From the NMR console TTL pulses were sent to the frequency generator PTS_1, which created the input pulses with carrier frequency of 300 MHz for the high-power amplifier HP_1 (Class AB amplifier, KALMUS, 500W Pulse, 150W CW). The output signal of HP_1 was used for the RF-pulse in NMR detection. In addition, from the NMR console gating TTL pulses were sent to the Pulse Delay Generator (PDG, Stanford Model DG535). Two channels of PDG were used. From the first channel a long TTL pulse was obtained to operate a relay. It allowed us to switch between the two power sources used for 300 MHz NMR detection (signal created by HP_1) at 7 T and for EPR pumping performed at $B=B_{pol}$ at a frequency ν_{irr} (signal created by HP_2, see text below). From the second channel of PDG a trigger pulse was sent to the input of the arbitrary waveform generator (AWG) (AWG2021, Sony Tektronix). At the output of AWG we obtained a train of pulses of length τ_p, repetition time τ_r and total irradiation time τ_{irr}. These pulses gate the frequency generator PTS_2 operating at a carrier frequency of ν_{irr} and driving the high-power amplifier HP_2 (Class A broadband linear amplifier, Electronic Navigation Industries Inc. (ENI) Model 5100L), whose output signal was used to perform the EPR pumping at the frequency ν_{irr} with the pulse sequence shown in Figure 7b. At the end of the EPR pumping cycle, the relay was switched from power amplifier HP_2 to HP_1 and synchronously the sample transferred to the detection field of 7 Tesla (corresponding to the 300 MHz NMR frequency of protons). Finally, the RF-pulse created by HP_1 was applied and the high-resolution NMR spectrum was recorded. Since pumping of the EPR transitions is done near the frequency of the NMR detection, our standard ^{1}H probehead could be used with slight modifications taking care of the fast electronic spin evolution. The main change is higher damping of the tank circuit to the extent that rise and fall time of the RF pulses is around 10 ns.

A new probe was designed consisting of a concentric two-coil arrangement to pump at 1.4 GHz frequency. The inner saddle shape coil is part of a 300 MHz resonance circuit for NMR detection (RF-coil) with its B_1 field orthogonal to that of the outer coil (degenerate saddle geometry, MW-coil) **[47]** that is used for EPR pumping at 1.4 GHz. The ground of the feeding line is decoupled from the coil by a small capacitor, reducing the influence of this coil on the RF circuit characteristics. The maximum B_1 achievable at 1.4 GHz is smaller by a factor of approximately 8 compared to 300 MHz due to the smaller filling factor of the outer coil with respect to the inner one and the lower output level of the 1.4 GHz MW amplifier (40 W TWT).

[Insert Table 2 here]

3.2. High-Field DNP Spectrometer (Frankfurt)

The High-Field DNP spectrometer was designed in Frankfurt for a magnetic field of 9.2 T, corresponding to a proton NMR frequency of 392 MHz **[48]**. The NMR detection is performed by a commercial Bruker Avance console. The cryomagnet can be swept by ± 40 mT, allowing optimizing the microwave resonance condition for the high power gyrotron microwave source, which operates at 258.9 GHz frequency. A microwave bridge was designed based on metal-dielectric waveguide technology (built by the Institute of Radiophysics and Electronics in Kharkiv, Ukraine) to pump the electron spin transition for DNP and EPR detection (Figure 9).

The bridge can switch between two microwave sources:

- a tunable solid state microwave source (45 mW, 255 to 263 GHz, VDI-S019b) for microwave cavity tuning, CW-EPR and test purposes

- a high power gyrotron source (4.7 T, 258.9 GHz frequency, tuning range 60 MHz, 20 W power, GYCOM) used for DNP excitation.

The probe is equipped with field-modulation coils for lock-in detection (Stanford Research SR510) for CW-EPR detection. The microwave bridge operates for EPR experiments in a Michelson-Interferometer configuration with a 3 dB beam splitter and equal length reference and signal transmission lines to balance the microwave reflection from the double-resonance structure (Figure 9). For DNP operation, the 3 dB beam splitter is replaced by a 24 dB coupler, which couples 99.5% of the microwave power to the cavity, and only 0.5% of the microwave power to the microwave detection diode (VDI-WR3ZBD-S027C). The overall losses of the microwave transmission system are below 2 dB. Spectral purity of the low power solid state source is defined by the 16-17 GHz YIG oscillator with a phase noise of -105 dBc/Hz (@ 10 kHz offset), multiplied by 16 according to the frequency multiplication chain. Therefore, the source fulfills the requirements necessary to conduct DNP and EPR experiments. The long-term frequency drift of the microwave source is about $4\text{x}10^{-6}$ per hour which is sufficiently stable to run an EPR experiment with nitroxide radicals for half an hour without an evident distortion of the EPR spectra. The high power gyrotron source is connected via a quasioptical corrugated waveguide system to the microwave bridge. The transmission line consists of 18 mm inner diameter corrugated waveguide pieces with a total length of about 14 m, and additional passive components, such as a calorimeter for power measurements, an attenuator, 90° bends, and a mechanical MW switch. The total losses are measured to be < 4 dB. The high power gyrotron frequency stability was tested by repeating EPR measurement of TEMPOL by sweeping of the main magnetic field and simultaneous detection of the magnetic field value via the water proton NMR signal. From such experiments the gyrotron frequency drift was estimated to be in the range of $6\text{x}10^{-6}$ 1/hour, which is again stable enough to perform reproducible DNP experiments with all the radical solutions we have investigated so far.

The most sophisticated part of the spectrometer is the double resonance structure for liquid solutions, consisting of a helix for RF excitation and NMR detection (400 MHz resonance frequency), which is the body of the cylindrical TE_{011} cavity for microwave excitation and EPR detection at 260 GHz. A similar design was described earlier for 140 GHz / 200 MHz **[19]**. The microwave cavity is completed by two plungers at each end of the helix made of KEL-F with flat caps coated with silver thin film. One plunger is moveable for microwave frequency tuning. Microwave coupling is achieved through an elliptical centered iris via a WR-4 waveguide that touches the helix in the middle, grounding the coil at this position with respect to RF. The angular electric field distribution of TE_{01n} modes is maintained since the gaps between turns are almost parallel to the surface currents. Moreover, the gaps serve as a filter of other unwanted modes, so that the cavity shows a clear microwave spectrum of only TE_{01n} modes. The resonance structure was simulated for frequency response, magnetic field distribution, and calculations of Q- factor as well as B_1 value using Ansoft HFSS simulation program (Figure 10). The MW cavity drastically reduces the MW electrical field strength at the sample position, thus avoiding excessive heating of the liquid sample; secondly, it enhances the MW magnetic field strength at the sample position about an order of magnitude. The conversion factor from microwave power P_{MW} to magnetic field strength B_{MW} has been determined by pulse EPR FID experiment on a fluoranthenyl hexafluorophosphate ($(FA)_2PF_6$) single crystal using a 200 mW orotron source (GYCOM, Russia). The amplitude of the FID signal was monitored as a function of pulse length, leading to an optimal pulse length of 80 ns for a $\pi/2$ pulse. This corresponds to microwave field amplitude of $B_{\mathrm{MW}} = 1.2$ G.

The NMR helix coil is tuned to 392 MHz proton frequency by a parallel capacitance C_{HT} and matched to the line impedance of the 50 Ω feeding line by the capacitance C_{HC}. We use an extra capacitance C_{HS} connected to ground to drive the coil symmetrically, e.g., to compensate for imbalance due to the RF coupling. In the case of a perfectly symmetrically driven solenoid the current is maximal in the center-turn corresponding to a virtual ground **[49]**. Thus, the RF field distortion due to the electrical contact between the grounded waveguide and the center-turn of the solenoid is minimized. The magnetic field inhomogeneity, caused by susceptibility mismatch rising from materials of the sample holder, plungers and the waveguide taper resulted in a broad NMR peak with a total line width of about 30 Hz. Excitation with microwaves caused additional heating of the sample, as can be seen from the NMR shift of the water proton line (Figure 11). This NMR shift served as a temperature gauge to determine the sample temperature with high precision (1 °C ~ 0.01 ppm shift), which is important for the DNP enhancement analysis. The DNP active sample volume is only 3-4 nl for 0.05 mm diameter capillaries, resulting in a small NMR filling factor.

[Insert Table 3 here]

3.3. *EPR Spectroscopy*

EPR characterization of the radicals has been performed with commercially available pulsed EPR spectrometers (Bruker ELEXSYS) at X-band (9 GHz / 0.3T), Q-band (34 GHz / 1T), W-band (95 GHz / 3.4 T) frequencies. Homebuilt spectrometers at G-band (180 GHz / 6.4 T) **[50, 51]** and at 260 GHz / 9.4 T **[48]** were used for the high-field characterization. DNP experiments at various magnetic fields ranging from 50 μT to 9.4 T have been conducted to quantitatively describe the field dependence of the Overhauser DNP efficiency. Aside from the novel DNP spectrometers described above, NMR detection was implemented to already exising EPR spectrometers working at 0.3 and 3.4 T in Göttingen. A further DNP setup in Frankfurt, constructed for other spacial resolved MRI applications and working at 1.5 T was also used to map the field dependence of liquid-state DNP.

A DNP setup was built in Göttingen for the experiments at 0.3 T (9.7 GHz EPR, 15 MHz ^{1}H NMR) **[52, 53]**. The DNP spectrometer described in Figure 12 consists of a commercial Bruker ELEXSYS EPR set-up equipped with a Varian TWT 20 W amplifier and a Bruker Minispec for NMR signal detection (2-65 MHz). Concomitant EPR excitation and NMR detection were accomplished in a dielectric ENDOR resonator with a probehead connected to external RF tuning and matching capacitors.

The B_1 microwave field was approximately 10 G at the maximum available power (20 W) sufficiently saturating one nitroxide hyperfine line of perdeutereated ^{15}N-TEMPONE at room temperature in a concentration range of 5 - 25 mM **[33]**. A field frequency lock is used to prevent off-resonant drifts of the magnetic field. The cavity absorption dip was stabilized by applying a constant flow of N_2 gas, dissipating heat from the cavity walls. More details can be found in **[53]**. The heating of the sample caused by microwave excitation was monitored via insertion of an optical fiber sensor into the sample and compared to the heating calculated from the observed reduction of the cavity quality factor due to the dielectric losses of the sample. Thus, the enhanced DNP effects introduced by heating of larger sample volumes could be quantitatively compared with the temperature dependence of the coupling factors, as predicted by NMRD experiments **[35]**.

For the DNP experiments at 1.5 T (42 GHz EPR, 63 MHz ^{1}H NMR) a home-built set-up in Frankfurt was utilized. The microwave power of 2 W was fed into a home-built TE_{011} microwave resonator through a slit shaped iris in the center of the cylinder body. The quality factor of the resonator is about 1600 loaded with a 0.3 mm ID capillary of the liquid TEMPOL/water sample. EPR detection was performed with a microwave detector diode; NMR and DNP detection were performed with a home-built NMR detection coil outside of the slit cylindrical microwave resonator, connected to a Bruker Minispec NMR spectrometer (described above).

For the investigation of DNP at 3.4 T (94 GHz EPR, 140 MHz ^{1}H NMR) a spectrometer was assembled in Göttingen **[52, 53]**. The set up is based on a pulse EPR spectrometer with a 400 mW power upgrade (Bruker ELEXSYS E680) and an Avance III NMR console (Bruker). Similar to the 9.7 GHz set up, an ENDOR probe head with additional RF tuning and matching devices was utilized. The length of the TE_{011} cylindrical resonator at 94 GHz is around 4-5 mm and its diameter is slightly larger than 4 mm. Such small dimensions combined with the limited penetration depths of the 94 GHz microwave in water (0.24 mm) restricted the sample size to 0.1 mm ID. Samples were irradiated by a microwave pulse for about 1 s and the subsequent NMR FID was recorded. The experiments were performed without active cooling, due to the restricted access of the gas flow into the cavity. We estimated the temperature by measuring the reduction of the cavity quality factor that yielded to an increase in temperature of about 15 K.

3.4. NMR Relaxometry

Longitudinal relaxation rates at magnetic fields ranging from 0.01 to 40 MHz proton Larmor frequency were measured using the field cycling technique with a high sensitivity Stelar Spinmaster FFC-2000-1T. According to this approach, a solenoid is used to turn the magnetic field on and off, with typical switching times of 0.1 milliseconds per MHz. The sensitivity of the instrument permits the detection of the protein proton magnetization for proteins of maximal molecular weight of 60-70 kDa dissolved in low to sub-millimolar concentration in D_2O **[54]**. Relaxation rates at fields below 15 MHz are acquired in the “prepolarized” mode: protons are prepolarized at 30 MHz and the magnetization decay curves at the relaxation fields are observed. Conversely, data above 15 MHz are acquired in the “direct” mode, i.e., by observing the magnetization buildup curves from zero magnetic fields up to the relaxation fields. The fit of the decay or buildup curves provide the longitudinal relaxation rates with an error below 1%. Proton nuclear magnetic relaxation dispersion (NMRD) profiles are obtained by plotting the proton relaxation rates as a function of the applied magnetic field. The probe shuttle DNP setup developed in Berlin was used for spectrally resolved NMRD measurements from 0-7 T, as described above **[55]**.

4. **Experimental Results**

In this concerted research on DNP enhancements in liquids, electron spin and nuclear spin relaxation rate field dispersions, as well as coherent and relaxation effects of hyperpolarized nuclear spin systems within the field shuttle process have been investigated in detail. For the first time the field dependence of the Overhauser DNP effect has been measured up to fields of 10 T. Together with NMR dispersion measurements and an EPR characterization of the electron spin relaxation and saturation they build the basis for a quantitative description of the field dependence of coupling factor ξ, leakage factor f and saturation factor s. Coherent and relaxation effects within the passage from the low polarization field to the high NMR detection field in the shuttle-DNP approach have been thoroughly experimentally investigated and theoretically modelled, helping to understand and optimize the DNP efficiency for the shuttle-DNP approach. Additionally, pulsed and coherent polarisation transfer methods have been investigated experimentally and theoretically, to further improve the DNP enhancements. These results, which build the basis for a thorough evaluation of the potential of liquid DNP at high magnetic fields, will be described in the following.

4.1. Saturation of Paramagnetic DNP Agents

Free nitroxide radicals are well-known in the field of EPR spectroscopy and regained interest with the introduction of site-directed spin labeling of proteins **[56]** for CW-EPR, PELDOR (Pulsed Electron Electron Double Resonance) **[57, 58]** as well as paramagnetic relaxation enhancement (PRE) applications in NMR **[59]**. Many of their properties, such as stability, covalent binding to cysteins and easy accessibility, make them the most commonly used and best characterized spin tags in biomolecular research **[60]**. We have therefore chosen nitroxides dissolved in water as our DNP agent/target system to experimentally probe the magnetic field dependence of the DNP effect in liquids. Unfortunately, both the isotropic and anisotropic part of the nitrogen hyperfine coupling (^{14}N: I=1, ^{15}N: I=1/2) complicates the experiment and quantitative determination of the saturation factor. The anisotropic part of the hyperfine coupling leads to very fast relaxation rates due to the rotational motion of the molecule. At high magnetic fields the anisotropy of the electron spin g-tensor adds to this and further increases the relaxation rates. Additionally the large isotropic nitrogen hyperfine splitting inhibits a resonant excitation of all EPR lines. However nuclear spin relaxation and Heisenberg spin exchange couple the hyperfine EPR lines at the high radical concentrations used for DNP, leading to a substantial cross-saturation of the other hyperfine transition **[28, 30]**. Different from radicals like trityl **[61]**, which consists of a single homogeneous or inhomogeneously broadened EPR line, a simple analytical approach as described in equation (5) cannot be used to calculate the saturation parameter. Theoretical descriptions of the electron spin saturation *s* were developed especially for nitroxides (S=1/2, I=1), including Heisenberg exchange, nuclear spin relaxation and rotational tumbling rates **[28]** and were recently extended for DNP based on a density matrix approach **[32]**. However, electron and nuclear relaxation rates, as well as Heisenberg exchange rates are required as input parameters.

Experimentally, ELDOR spectroscopy can be used to determine the cross-saturation of the second hyperfine line (for ^{15}N) and therefore the saturation parameter *s*. This was performed at X-band frequencies (9 GHz, 0.3T) on perdeuterated TEMPONE-^{15}N **[33]**. The pulsed ELDOR experiment consists of a saturating pump pulse followed by a detection pulse and FID detection. The probe pulse frequency was set resonant to one of the two nitroxide hyperfine lines, whereas the pump pulse frequency was swept over the other hyperfine line. A reduction in the FID was observed when the pump pulse frequency was resonant with the second hyperfine line, which directly corresponded to the saturation level of this line. For 25 mM perdeuterated TEMPONE-^{15}N in aqueous solution, the total saturation of the electron spin system resulted to a saturation of s = 0.9 under the given experimental conditions **[33]**. The pulsed ELDOR experiment also allowed to independently determining the Heisenberg spin exchange and the T_1 relaxation rate of the electron spin system.

4.2. Field Dependence of DNP Enhancement

DNP Experiments were performed at 300 MHz, 1.4 GHz, 9 GHz, 45 GHz, 95 GHz and 260 GHz EPR resonance frequency and the corresponding magnetic field values. For the first time, systematic studies of the frequency dependence of Overhauser DNP have been carried out over such a broad frequency/field range. The experimentally observed enhancement factors ε and other relevant parameters of the experiments are collected in Table 4. It is evident that considerable enhancements up to two orders of magnitudes have been achieved over the accessible frequency range. The DNP enhancements at fields ≥ 3 Tesla have been reported within this consortium for the first time. Much effort has been put into optimizing the DNP conditions at every frequency/field position, for example the enhancements obtained at X-band frequencies are about a factor of 2-3 larger than the values reported in several previous studies **[6, 40]**. It is of importance, as only in this case meaningful estimates of the coupling factor and its field dependence can be obtained (note that every data point represents a different experimental setup!). The obtained values show experimentally observed enhancements close to the maximum value at low magnetic field values and unexpected high enhancements even at magnetic fields above 1.5 T.

Despite the fact that all the tabulated DNP experiments have been performed under optimal conditions and, in many cases, with the highest ever observed enhancements, it should be kept in mind that especially the saturation factor s will still be below 1 for almost all frequencies. Especially at high microwave frequencies it is extremely difficult to saturate the nitroxide spin system at room temperature. Additionally, at such high frequencies it is impossible to measure electronic relaxation rates independently by pulsed EPR methods as mentioned above for X-band frequencies. Therefore, the experimental observed enhancements at higher microwave frequencies are expected to be well below the maximum achievable DNP enhancements ε_{max} , which would be reached for $f = 1$ and $s = 1$. One way to overcome this problem is to plot the inverse DNP enhancement $1/\varepsilon$ as a function of the inverse microwave power $1/P_{mw}$, as shown in Figure 13 for two nitroxide radicals measured at 260 GHz/ 9 T **[62]**.

Extrapolation of the linear curve to infinite MW power allows in principle the determination of ε_{max} without prior knowledge of the saturation factor *s*. Unfortunately, this method is difficult to apply at high magnetic field values, as can be seen from Figure 13. Increasing the microwave power on the sample unavoidably leads to additional sample heating. Especially for the small sample volumes used at high microwave frequencies, this heating power will rise the sample's temperature and therefore change the parameters, affecting all factors contributing to the DNP enhancement (equation 2). In particular the coupling factor, which shows a strong nonlinear dependence of the correlation times at high magnetic fields, will be strongly changed by temperature. Therefore, the temperature has to be monitored independently (and ideally has to be kept constant). At high magnetic fields the temperature dependence of the water protons chemical shift could be used to estimate the temperature rise of the sample by microwave irradiation.

4.3. Field Dependence of Nuclear Relaxation Rates

An independent estimate of the coupling factor ξ can be obtained by measuring the water proton relaxation rate of a solution containing TEMPOL **[52]** or TEMPONE **[35]** radicals as a function of the magnetic field, as shown in Figure 14.

The paramagnetic enhancement of water proton relaxation rates results from the sum of outer-sphere and inner-sphere contributions. Outer-sphere relaxation is due to the dipolar interaction between unpaired electron(s) and protons of freely diffusing water molecules. It is described by the diffusion constant and the distance of closest approach **[37]**. Inner-sphere relaxation is due to the dipolar and contact interactions between unpaired electron(s) and protons of water molecules transiently bound to the paramagnetic molecule, or belonging to the paramagnetic molecule itself, in exchange with bulk water protons. In the absence of ZFS, it is described by the Solomon-Bloembergen-Morgan (SBM) equation **[26, 63]** through the number of coordinated water molecules and their distance from the unpaired electrons, the contact coupling constant and dynamic parameters, as the molecular reorientation time τ_r, the electron relaxation time and the lifetime of coordinated water protons. In radicals, the contact coupling constant is negligible and the electron relaxation time is relatively large. Therefore, the inner-sphere relaxation is dominated by the dipolar interaction, modulated with a correlation time τ_c provided by the inverse of the sum between the reorientation rate, τ_r^{-1}, and the exchange rate, τ_m^{-1} ($\tau_c^{-1} = \tau_r^{-1} + \tau_m^{-1}$). The coupling factor can be calculated from Eq. (6) as:

$$\xi = \frac{5}{7}\left[1 - \frac{3kJ(\omega_I,\tau_c) + 3k'J_t(\omega_I,\tau_t)}{R_{1\mathrm{para}}}\right] \tag{9}$$

where k is a constant related to the inner-sphere dipolar relaxation, $J(\omega,\tau)$ is the Lorentzian spectral density function, k' is a constant related to the outer-sphere relaxation, τ_t is the diffusion correlation time (Equation (7)), $J_t(\omega,\tau)$ is described by Eq. (8), and $R_{1\mathrm{para}}$ is the paramagnetic enhancement of the nuclear relaxation rate.

The analysis of the relaxation rate profiles as a function of the applied magnetic field can provide a direct estimate of the coupling factor. In fact, R_{1para} can be directly measured and the $3kJ(\omega_{I,}\tau_c)+3k'J_t(\omega,\tau)$ term can be estimated from the observed field dependence of the relaxation rates.

A very good fit of the relaxation profiles of TEMPOL and TEMPONE water solutions could actually be obtained when both inner-sphere and outer-sphere contributions were considered **[35]**. The contribution of inner-sphere relaxation amounts to about 25% of the total relaxation rate at low magnetic fields. The value of the diffusion coefficient D (2.9×10^{-9} m^{2}s^{-1}), obtained from the fit of the NMRD curve, corresponds to the expected value at 298 K. The distance of closest approach (2.7 Å) is somewhat larger than expected for the distance between the unpaired electron (delocalized between the nitrogen and oxygen positions) and the water proton in a hydrogen-bound position. However, since the radicals are not spherical and the unpaired electron is not located at the center but close to the border of molecular surface, the actual distance of closest approach is different depending on the direction from which water molecules approach the nitroxides, and the calculated value represents a weighted average. The diffusion time obtained from the distance of closest approach and the diffusion coefficient is 26 ps (formula 7), quite similar to the value obtained for the correlation time τ_c modulating the inner-sphere dipolar relaxation of 20 ps. If two inner-sphere water protons are considered, their distance from the unpaired electron provided by the fit is 3.0 Å. The coupling factor at 15 MHz (0.3T) calculated from the above parameters and Eq. (9) results to $\xi = 0.35 \pm 0.02$ **[52, 35]**. When the temperature increases, the coupling factor also increases as a consequence of the shorter correlation times. Temperature dependent NMRD measurements gave coupling factors ξ of 0.39 (308K), 0.41 (318 K) and 0.43 (328K) for TEMPONE at a proton frequency of 14 MHz (0.3 T). From the best fit parameters to the NMRD curves, ξ values could also be calculated for 140 MHz proton frequency (3.4 T), and resulted to be 0.05 (298 K), 0.09 (308 K), 0.11 (318 K) and 0.14 (328 K) **[35]**. These results demonstrate the increased sensitivity of coupling factor (and therefore DNP enhancement) on the temperature at high magnetic fields.

4.4. Coupling Factor from Molecular Dynamics Calculations

For the first time we used molecular dynamic (MD) simulations as an alternative approach to stochastic models for the translational and rotational motion of the DNP agent and target molecules. From such trajectories, dipolar spectral density functions and coupling factors were calculated for different temperatures (Figure 15). The calculated values from MD give higher coupling factors than the classical stochastic force-free approach, which is most obvious at high magnetic fields **[64]**. The coupling factors deduced from MD simulations decrease only with $\omega_S{}^{-1}$ compared to the classical models which predict $\omega_S{}^{-2}$ for rotational motion and $\omega_S{}^{-3/2}$ for translational motion.

4.5. Coherent Polarization Transfer Effects within the Shuttle Process

Since in field-shuttling DNP experiments field variation over a wide field range is always a necessary step, it becomes important to understand the spin dynamics of the polarized systems at arbitrary magnetic field strength. In particular, it is quite common that the polarized spins have a network of spin-spin interactions (scalar or dipolar) in the molecule that affects their evolution. We have studied two types of spin evolution of the coupled multi-spin systems: polarization transfer among coupled spins and longitudinal relaxation behavior. Both effects should inevitably be taken into account for quantitative interpretation of the low-field DNP data. Polarization transfer effects also become important as they potentially allow one to enhance the NMR lines belonging to spins, which cannot be polarized directly. Longitudinal relaxation is a process which occurs during the passage over a broad field range and results in a decrease of the overall polarization. Our studies open new insights into spin evolution of the multi-spin systems at variable field, helping to develop new strategies for optimizing the polarization transfer, making it selective and efficient and minimizing the relaxation losses during shuttling. In particular, the involvement of so-called long-lived spin states has been investigated **[65]**.

It turns out that polarization transfer and relaxation phenomena in the coupled multi-spin systems have much in common. The key feature of all kinds of spin evolution at variable magnetic field is the transition from weak to strong coupling of spins when the magnetic field is being decreased **[66]**. The *i*-th and *j*-th spin are termed weakly coupled once their spin-spin interaction J_{ij} is much smaller than the difference in their Zeeman interactions, ν_i and ν_j, with the external magnetic field ($J_{ij} << \nu_i - \nu_j$), otherwise they are coupled strongly. Since the ν_i are proportional to the external field the strong coupling situation can always be met by appropriate lowering of the field. For protons with typical values of their chemical shift and scalar spin-spin interaction the condition of strong coupling can be fulfilled for magnetic fields up to several Tesla; only for hetero-nuclei it becomes necessary to go to very low field. Strongly coupled spins have collective (entangled) energy levels, for instance, two strongly coupled spins have singlet and triplet eigenstates instead of the Zeeman states, in which both spins are fully characterized by their projections onto the field axis. Consequently, strongly coupled spins tend to be polarized together and to relax together with a common T_1 time.

We have performed detailed experimental and theoretical studies of the polarization transfer and relaxation effects in coupled multi-spin systems over a wide field range. We developed a theoretical approach to both problems under consideration that very well explains the experimental findings. As far as the polarization transfer among coupled spins is concerned there are the following three main statements resulting from the nuclear spin-spin interactions **[67]**:

(1) Strongly coupled spins get polarized together: once one of them is directly polarized carrying the longitudinal spin order $\langle I_z \rangle$, its polarization is shared with the others. This effect is absent for weakly coupled spins (high-field case). Such an effect can lead even to long-range polarization transfer among spins, who have no direct couplings but are linked via spacer spins by a chain of interactions. Once every spin is strongly coupled to its neighbor, the entire spin system gets polarized.

(2) Polarization is shared among the coupled spins on the timescale of their inverse J-couplings. Such a transfer is a coherent process: there are quantum beats in the transfer kinetics and its rate and efficiency far exceed those given by cross-relaxation. Thus, for efficient transfer it is necessary that the timing of experiment is set properly: the sum of the residence time at low field and the time of field switching to the high detection field has to be larger than $1/J$. On the other hand, when one wants to know the initial spin polarizations,

which existed before the polarization transfer occurs, the sum of these times must be much smaller than 1/*J*.

(3) In the field dependence of polarization there are pronounced sharp features, which are caused by avoided crossings of the nuclear spin levels at distinctive field positions, which are determined by the chemical shifts and coupling constants of the interacting spins. At such crossing points the polarization transfer efficiencies have their extremes, which results in particularly selective and efficient polarization transfer between certain spins. Such features should not be misinterpreted, i.e., erroneously attributed to the peculiarities of the polarization process at this field.

Finally, manifestation of all the effects mentioned here strongly depends on the speed of field switching from the polarization field to the high detection field. Our studies have revealed pronounced differences between the two limiting cases of very slow (adiabatic) and very fast (sudden) field switching. For numerical modeling of the real experimental data it becomes necessary to take the actual profile of field shuttling, otherwise the results may not agree quantitatively with the experimental data.

The concept of hyperpolarization (HP) transfer among strongly coupled spins has been applied to transfer CIDNP in amino acids **[44]**. CIDNP was created photo-chemically in reactions of excited dyes with amino acids. We achieved highly efficient CIDNP transfer among the aromatic protons of tryptophan in the vicinity of the level anti-crossings. In particular, highly selective HP transfer between the H4 and H7 protons (Figure 16) has been observed although they have nearly zero direct spin-spin interaction, but are coupled via the H5 and H6 protons, which play the role of the spacer spins.

At low field HP can be transferred over the entire spin system of all four protons, which form a strongly coupled spin system. HP effects were shown to be strongly dependent on the speed of field-cycling. In tryptophan coherent CIDNP transfer has been reported at very low magnetic fields (<10 μT), which are due to strong coupling of protons and fluorine. CIDNP transfer kinetics contain an oscillatory component, which is a clear indication of coherent nature of the process (Figure 16). Modeling of such effects will allow one to optimize the experimental parameters for efficient and selective transfer HP in biologically important molecules. Moreover, HP transfer to hetero-nuclei with long relaxation times can be of importance in NMR spectroscopy and imaging.

4.6. Relaxation Effects within the Shuttle Process

T_1-relaxation is often a major limiting factor in field-cycling DNP experiments and has much in common with the coherent polarization transfer phenomena described above. Our study has revealed well-pronounced effects of spin-spin couplings on the field dependence of the T_1-relaxation times. Firstly, scalar coupled spins having completely different high-field T_1 times tend to relax at low field with a common relaxation time. Secondly, the NMRD curves exhibit sharp features such as peaks, dips and steep steps at the fields corresponding to the positions of nuclear spin level anti-crossings. Such effects of spin-spin couplings show up not only for individual spins but also for the T_1-relaxation of the total spin magnetization of the molecule. The influence of spin-spin coupling is of importance, as long as the coupling strength J is larger than the inverse T_1-relaxation time of the spins. Around $J \cdot T_1=1$ there is also a coherent contribution to the relaxation kinetics, resulting in an oscillatory component of the magnetization curves **[68]**.

We have studied a set of amino acids (histidine, tyrosine, tryptophan, methionine, aspartic acid) **[55]**, purine nucleotides (adenosine mono-phosphate and guanosine mono-phosphate) **[69]** and several other compounds with the result that our theoretical modeling has been fully confirmed. The study was site-specific; meaning that the T_1 relaxation times of protons were obtained for individual spins and not only for the molecule as a whole. Most of these molecules have small size and high mobility so that their correlation times are very short and the approximation of extreme narrowing is fulfilled for the relaxation rates in the whole accessible field range. In such a situation the relaxation rates are field dependent only because of the interactions among the spins. While at high fields the individual spins have distinctly different T_1 times, their scalar spin-spin interaction fulfills at low field the condition of strong coupling and leads to convergence of their T_1 dispersion curves. In addition, a coherent contribution to the relaxation kinetics has been found, which is due to the coupling between spin polarization and coherence in the relaxation process. As a consequence, in such cases the NMRD curves do not directly reflect the spectral density function of the motional processes as it is usually assumed, but the effects of coherent motion and spin coupling must be separated for a reliable evaluation (Figure 17).

Relaxation processes in proteins at variable field are of particular importance for potential applications of DNP for biomolecular structure determination. Therefore, also relaxation effects in protein molecules have been studied by NMRD. In fact, in shuttle DNP experiments an effective DNP enhancement can be obtained only if the polarization achieved at the low field EPR, where proton spins are polarized, is not lost during the transfer to the high magnetic field, where high-resolution NMR measurements can be performed **[45]**. Relaxometric measurements on proteins dissolved in D_2O provide direct access to the relaxation rates of non-exchangeable protein protons down to very low magnetic fields. The relaxation rate of each protein proton depends on the distance from all neighboring protons and on the correlation time modulating the dipolar interactions. For folded diamagnetic proteins, a distribution for the relaxation rates was obtained, which mainly depends on the size of the protein through its reorientation time and on the extent of the internal motions, represented by a collective order parameter S_C^2 **[54, 70, 71]**. Figure 18 shows the collective protein proton relaxation rates measured for the proteins lysozyme (with a molecular weight of 16 kDa) and albumin (64 kDa). It can be seen that the low field relaxation rates can be as large as hundreds/thousands of s^{-1}. Even protons of proteins with reorientation time as small as 5 ns (protein molecular weight of 10-15 kDa) have relaxation rates of the order of 100 s^{-1}, indicating that magnetic field drops must be avoided to retain polarization during shuttling between the EPR to the NMR cavity **[45]**.

Therefore, fast shuttling is needed to limit the polarization losses and achieve the most uniform enhancement over all molecular sizes but, even more importantly, relatively strong magnetic fields during sample transfer are necessary.

It was necessary to consider in detail the nuclear longitudinal relaxation in the course of field variation also for the quantification of these losses and correct interpretation of the DNP data. When the DNP experiments are done at low field giving a certain value of nuclear polarization, M_{in}, the enhanced NMR signals allow one to determine only the final polarizations M_{fin} at high field. To obtain the initial polarizations M_{in} and thus the DNP enhancements ε it becomes necessary to solve the inverse problem and to take the relaxation during field shuttling into account. We modelled the relaxation effects numerically and calculated the nuclear polarization, M, from a Bloch equation with field dependent relaxation and equilibrium polarization

$$\frac{dM}{dt} = -R_1^n(B)(M - M_0(B)) \tag{10}$$

Here $M_0(B)$ is the equilibrium polarization at the magnetic field B, which is proportional to B, while $R_1^n(B)$ is the field-dependent rate of the longitudinal nuclear spin relaxation. The maximal value of M_0 defined as M_{max} corresponds to the equilibrium polarization at our detection field of 7 Tesla. To solve this equation we have taken the actual profiles $B(t)$ of field variation and the $T_1(B)$ relaxation dispersion curves measured individually for all spin positions in the molecules. The $R_1^n(B)$ curves we fitted by the Redfield-type functions

$$R_1^n = R_a + \frac{R_b}{1+\alpha B^2} \tag{11}$$

to interpolate the relaxation dispersion in the whole field range. Using these relations, we calculated the polarizations, M_{fin}, at the end of the field variation period as a function of the initial polarization, $M_{in}=M(t=0)$. The procedure was cross-checked by systematic experiments.

The decay of magnetization during sample transfer from the low magnetic field, at which the DNP occurs, to the high magnetic field, at which the detection takes place, has been measured for glucose and ubiquitin. During shuttling of aqueous glucose solution from the center of the NMR magnet up to 1.5 m and then down again as soon as possible, only about 30% of the initial magnetization is lost. Assuming that the magnetization loss factor is the same for shuttling up as well as for shuttling down the magnetization after the planned EPR→NMR shuttle process will be approximately 84% of the initial magnetization. Shuttling ubiquitin in the present setup (1.5 m shuttle distance, 0.7 bar pressure) will result in magnetization losses of about 55% (one direction) on methyl groups due to sample transfer. The T_1 relaxation time of the methyl groups at 1.5 m (1.5 mT) was estimated from experiments to be around 30 ms or longer. Other groups show much severer relaxation during sample transfer. Less loss due to relaxation is expected when the EPR magnet is added on the top of the shuttle DNP spectrometer due to the additional magnetic field on the sample path. As the correlation time of methyl groups of large proteins is fairly independent of the rotational correlation time of the protein itself, we expect that even larger proteins than ubiquitin can be shuttled without major magnetization losses on the methyl groups.

4.7. DNP Enhancements with Sample Shuttling

Based on the above findings the sample shuttle DNP setup with fast shuttle time and a two-center magnet was designed. The first DNP experiments were performed on small molecules which can be dissolved in sufficiently high concentration to obtain a sizeable Boltzmann signal to compare with **[43]**. We report results on water, DSS, ethanol and glucose. Ethanol is only slightly larger than water, therefore easy to polarize, and shows only modest relaxation losses during shuttling. The multiplet structure of the peaks give insight into the resolution obtained taking shuttling and the radical induced line broadening into account. Glucose is a larger molecule and therefore shows larger relaxation losses in comparison to water, ethanol and DSS allowing to explore the limits of this shuttle DNP set-up. Even larger biomolecules are presently under investigation.

We used a 5 mM TEMPONE-D,^{15}N solution (80/20 H_2O/D_2O) with 10 mM DSS and 0.1 M ethanol. This concentration is a compromise between kinetics of transfer and proton relaxation during shuttling. Larger concentrations would lead to larger relaxation losses (see Figure 14). In order to minimize relaxation losses during shuttling transfer, the time between the low-field and the high-field positions was minimized to t_{sd} = 37 ms. Mechanical oscillations after the arrival of the sample at 14 T were allowed to decay during an additional delay t_{psd} = 70 ms. For saturation, we used the low field EPR line, whose resonance frequency had been optimized by a series of short shuttle-DNP experiments. In these experiments, the B_0 field was set to the low field line and changed in steps of 0.4 G, until the maximum enhancement was observed. For this optimization procedure a short irradiation time of 1 s at a low microwave power of 10 W was sufficient. The maximum enhancement factor for ethanol was measured to be ε^{HF} = - 1.7 (Figure 19) calculated from the ratio between the integral of the respective signal with and without DNP. (Table 5).

For the DNP experiment the sample was shuttled from the high-field to the low-field position. The microwave was irradiated for 12 s with a power of 16 W. Directly after the microwave irradiation (tppd = 0 s), the sample was shuttled back to the high-field position (ts = 40 ms) and after a settling time of tpsd = 70 ms, the detection pulse was applied. Note that in addition to the H_2O proton, also the proton signals from the ethanol and the

DSS reference show a negative enhancement. The shift and broadening of the water peak is caused by microwave heating. For the selected regions, the enhancement factors determined from the integrals are given in Table 5.

The same measurement conditions were then used for a 10 mM TEMPONE-D,^{15}N solution in 99.8% D_2O with 5 mM DSS and 0.5 M D-glucose. The water, DSS and the D-glucose protons show a negative enhancement (Figure 20). We achieved an enhancement factor in the range of ε^{HF} = -1.4 to -2.8 for the different protons of the D-glucose (Table 6). We estimate relaxation losses for the glucose protons due to longitudinal T_1 relaxation between the low field and the high field between 10 % and 30 %. With these promising results for glucose, higher molecular weight systems are currently under investigation in our laboratories.

4.8. Pulsed Polarization Transfer Methods

We studied the efficiency of polarization transfer from the electronic to the nuclear spin reservoir in liquid-state DNP using pulsed pumping of EPR transitions **[72]**. The primary aim of these studies was to develop strategies for minimizing the heating of the samples. It is a common problem in CW-DNP that, for reaching considerable saturation factors, high MW-power has to be exerted on the sample, resulting in heating. Besides this, it is often difficult to maintain high power for pumping the EPR transitions continuously over a long period of time. One of the ways to tackle this problem is exciting the EPR transitions with short intensive pulses with considerably long delays between them. As a consequence, the duty cycle can be kept low also providing reasonably low total power of pumping. This approach also has the potential of exciting several or all lines in the EPR spectrum if working with a sufficiently high B_1 pulse field strength. A necessary requirement is that the parameters of the pulse sequence are appropriately adjusted for optimal DNP enhancement. When optimizing the parameters of the pulse sequence one should rely on the coherent motion of the electron spins in the B_1-field during the pulse. Thus, setting the proper pulse length it is possible to flip the electron spin, which then relaxes during a relatively long time, which can be of the order of the electronic T_1 relaxation time.

A corresponding theory of DNP in the pulsed pumping mode has been developed that considers a simple pulse sequence. The pulse sequence of EPR pumping, which was used to produce the DNP effects, is shown in Figure7. A periodic train of pulses was applied with pulse length of τ_p and delay between the pulses equal to τ_r; accordingly the duty cycle (DC) of this sequence can be defined as DC=$\tau_p/(\tau_p+\tau_r)$. In the theoretical treatment of the problem it was assumed that the number of pulses was very large: this well describes the experimental situation since the duration of each cycle ($\tau_p+\tau_r$) is of the order of the electron spin relaxation times, whereas the whole duration of the pulse sequence is of the order of the much longer nuclear relaxation times. This is necessary for accumulating substantial nuclear polarization. Using such a scheme one can assume that the electron spin magnetization vector right before applying the pulse is exactly the same as after the subsequent cycle (pulse-delay). As a consequence, per each cycle of the pulse sequence the electron spins give exactly the same amount of polarization to the nuclei and the rate of polarizing the nuclei can be calculated. Under these assumptions a general formula for the DNP enhancement in the pulsed mode of pumping was obtained:

$$\varepsilon = \frac{I_z}{I_z^0} = \frac{1}{I_z^0} \cdot \frac{W_z \cdot T_1^n}{\tau_p + \tau} = \xi \cdot f \frac{\gamma_e}{\gamma_n} \frac{1}{N} \sum_{i=1}^{N} F_i(\omega_1, \delta\omega_i; T_1, T_2; \tau_p, \tau) \qquad (12)$$

In this formula the analogy with the CW-case can be easily seen: the enhancement is of the order of magnitude of the ratio of γ_e and γ_n; it is proportional to the coupling and leakage factors, whereas the saturation factor is replaced by its pulse analogue. The quantities F_i are different for individual lines of the spectrum (their total number is N) and depend on the amplitude of the B_1 field, frequency off-set between a given line and the MW-field, the parameters of the pulse sequence and the electron relaxation times. While the general expression is rather cumbersome, it reduces, if $\tau_p << \tau_r$ and $T_{1e}=T_{2e}=T_e$, to $F=\frac{1}{x}\cdot\frac{(1-\cos\varphi)(1-e^{-2x})}{1-2e^{-x}\cos\varphi+e^{-2x}}$ with $x=\tau/T_\mathrm{e}$ and $\varphi=\omega_1$ **[72]**. The formula obtained predicts an oscillatory component in the dependence of the enhancement on the pulse length resulting from the coherent motion of the electron spins in the B_1 field. Polarization maxima in the dependence on the pulse length correspond to flip angles φ of the electronic spin magnetization being odd multiples of π. Theory predicts damping of the oscillations at long τ_p due to the electron spin relaxation during the pulse, which results in lowering of the DNP effect. Maximal enhancements achievable in the pulsed mode are nearly the same as in CW-mode and are reached when π-pulses are applied. By properly setting the times τ_p and τ_r, one can fulfill the conditions that (i) DNP enhancement is high and (ii) DC is low. It is mandatory that the B_1-field is sufficiently strong $\frac{2\pi}{\gamma_e T_e} << B_1$ ($\tau_p << T_e$), whereas the delays can be as long as T_e, i.e., DC<<100 %. The condition of strong B_1 is the same as for cw-mode (required to achieve saturation factors close to 1/N); thus, one should be able to achieve nearly the same enhancements in the pulsed experiments with much lower total power. A similar approach was also used for DNP of inhomogeneously broadened EPR lines of one-dimensional organic conductors at 5 T magnetic field strength **[73]**.

Experiments done at two frequencies (300 MHz and 1.4 GHz) are in good agreement with the theoretical predictions. In these experiments the duration of each pulse, τ_p, was varied from 5 ns up to 25 μs allowing us to change the flip angle, φ, of the electronic magnetization over several periods. Assuming that the high field approximation is sufficiently precise at the low B_pol, we used standard Bloch equations, i.e., a flip angle $\varphi=\gamma_e B_1 \tau_p$ where B_1 is the amplitude of the co-rotating field component. The RF pulse shape was checked via a pickup antenna positioned near the RF coil and monitored by a digital oscilloscope. For 300 MHz B_1 of the pumping was calibrated by measuring the length of a $\pi/2$ pulse for protons at B_0=7 T. In all cases we used relatively short times τ_p in order to minimize effects by the electronic longitudinal and transverse relaxation times, T_1^e and T_2^e respectively. The duty cycle, DC, was varied in the range 1% ≤DC≤50%.

In comparison with CW pumping, a substantial gain in polarization was achieved. This is demonstrated in Figure 21, where the DNP amplitude is plotted as a function of the width of the pumping pulse, while the average pumping power (power amplitude × duty cycle) is kept constant. At pulse duration τ_p, corresponding to flip angles of odd multiples of π, the DNP efficiency goes through a maximum, showing that coherent electronic spin motion can be exploited. Because of B_1 inhomogeneities and relaxation effects the π-pulse yields the highest efficiency. For optimum power utilization the pulse repetition rate t_r^{-1} should be smaller than the electronic spin-lattice relaxation rate T_{1e}^{-1}.

When analyzing the resulting variation of ε as a function of τ (Figure 21, right) by means of eq. (12), the value of $T_{1\mathrm{e}}$ can be obtained. The best fit (solid line in Figure 21) gives us $T_{1\mathrm{e}}$=320 ns. The fit in Figure 22 is almost perfect, showing even that at small x the effect turns to a constant level, as expected for $\tanh(\frac{x}{2})/\frac{x}{2}$ (see eq. 12). The residuum is smaller than the experimental error margin and is seen only in a logarithmic plot.

Enhancements obtained for 1.4 GHz frequency of pumping are considerably lower because of the lower B_1 fields available.

4.9. Coherent Polarization Transfer Methods

The above described DNP experiments all involved polarization transfer driven by cross relaxation processes. On the other hand, coherent cross polarization using pulsed DNP should not show the same magnetic field dependence and promises larger polarization transfers at high fields. Unfortunately, the classical polarization transfers, where the Rabi nutation frequencies of the two coupled spins must be equal, $\gamma_I B_{1I} = \gamma_e B_{1S}$ **[74],** is not feasible for electron-nuclear spin systems. For electron spins B_{1e} > 0.1 mT is necessary to excite the full EPR line and efficiently drive the electron spin resulting in an unrealistic high RF field strength of B_{1I} = 0.066 T for protons!

Nevertheless, a number of methods involving coherent transfer pathways have shown promising results for solid-state DNP applications in the past. Nuclear orientation via electron spin locking (NOVEL) is a DNP method that achieves the HH condition between the electrons in the rotating frame and the nuclear spins in the laboratory frame **[75-77]**. A variant of the NOVEL technique is the integrated solid effect (ISE) **[78, 79]**. ISE uses continuous microwave irradiation and a fast field sweep through the EPR line, thereby rotating all spins through the HH condition. Another method is called rotating frame DNP, and was first demonstrated by Bloembergen and Sorokin on a single crystal of CsBr **[80]**. In this method, the cross effect (CE) and thermal mixing (TM) are performed in the rotating frame **[81-83]**. Finally a promising method is the dressed-state solid ef*fect* (DSSE) **[84-86]**, which is also known as electron-nuclear cross polarization (eNCP) **[84, 85]**. This method does not rely on non-secular hyperfine couplings and therefore should also be applicable in liquids.

In order to explore the potential of coherent transfer schemes for liquid state DNP experiments, a number of simple model systems consisting of one electron spin and one or two adjacent nuclear spins were studied theoretically, using tools based on optimal-control theory. The GRAPE (gradient ascent pulse engineering) algorithm **[87, 88]** was used to explore the physical limits of coherent time-optimal and relaxation-optimized electron-nuclear polarization transfer methods. This approach makes it possible to efficiently optimize tens of thousands of pulse sequence parameters and the resulting pulse sequences are not limited to previously known transfer schemes. Furthermore, experimental constraints and imperfections, such as limited RF and MW amplitudes, RF and MW field inhomogeneities, and resonator bandwidths can be taken into account. Finally, the analysis of the numerically optimized pulse sequences can provide insight into the corresponding transfer mechanism.

A first application of this approach was a generalization of the eNCP sequence **[84, 85]**, where polarization transfer was considered between one electron spin S and one nuclear spin I, where both relaxation and cross relaxation are neglected. Simulations of the transfer efficiency as a function of the frequency offsets from resonant excitation of spin S and I revealed a new eNCP matching condition that was previously unknown **[86]**. Furthermore, the GRAPE optimization of arbitrary time-dependent MW and RF fields allowed us to explore the physical limits of the maximum possible transfer efficiency as a function of transfer time. Figure 22 shows two examples of so-called TOP (time-optimal pulse) curves **[89, 90]** for electron-nuclear polarization and coherence transfer, where a transfer efficiency of 1 corresponds to an enhancement factor of γ_e/γ_H = 658 if the nuclear spin I represents a proton spin.

The time-optimal pulse sequences for transfer of electron polarization S_z to nuclear polarization I_z are reminiscent of selective population inversion (SPI) experiments **[91]**. However, in the time-optimal pulse sequences, RF pulses are applied simultaneously in contrast to conventional SPI-type pulse sequence, where the MW and RF pulses would be applied sequentially. The minimum time for full polarization transfer is limited by 1/2 of the inverse RF amplitude, corresponding to 25 μs for the example shown in Figure 22. As also shown in the Figure, the minimal time to achieve maximum transfer to transverse nuclear spin magnetization I_x is significantly shorter for the same maximum RF amplitude **[86]**. In this case, cw RF irradiation is simultaneously applied to both components of the nuclear hyperfine doublet, whereas only a single line of the hyperfine doublet is irradiated for the transfer to I_z.

In practice, relaxation effects have to be taken into account and the GRAPE algorithm can also be used to study the competing effects of coherent transfer, cross relaxation and auto relaxation **[86]**. For complex systems with a network of different hyperfine coupling constants, relaxation and cross-relaxation rates, simple transfer schemes are in general not able to take full advantage of the possible transfer mechanisms. By non-trivial combinations of incoherent and coherent transfer schemes, significantly improved transfer schemes are possible. As a first step in this direction, idealized model systems consisting of one electron spin coupled to one ^{15}N (or ^{1}H) spin and one additional ^{1}H spin in various geometrical arrangements and for a range of correlation times and resulting relaxation rates were investigated **[92]**. Although the considered spin systems were very simple and still far from systems that are relevant for practical DNP applications, a detailed analysis of the interplay between coherent and incoherent transfer mechanisms was possible and various combinations of coherent and incoherent transfer schemes were found. Coherent and incoherent transfer mechanisms can be distinguished by the presence or absence of bilinear (and higher order) density-operator terms, which provide characteristic signatures in numerical simulations of the spin dynamics. Both hyperfine couplings and cross-correlated relaxation effects provide efficient alternative and complementary transfer routes to Overhauser transfer, which can be simultaneously exploited using the GRAPE algorithm. In most three-spin model systems, optimal control pulse sequences provided significantly improved transfer efficiency to the nuclear target spin (e.g. ^{1}H) compared to conventional Overhauser schemes based on saturation or selective inversion of the electron spin. An example of a TOP curve for one of the three-spin model systems is shown in Figure 23, where a full enhancement is reached after about 30 μs in the presence of hyperfine couplings (solid curve and solid squares). In the absence of hyperfine couplings, i.e. when only incoherent polarization transfer is possible, significantly smaller enhancement factors can be achieved. For short and long transfer times, the corresponding incoherent TOP curve, represented by open squares, is closely approached by Overhauser experiments based on inversion (dashed curve) or saturation (dotted curve) of spin S, respectively.

Although the system parameters for the simple two and three spin systems that were studied by optimal control methods so far are not very realistic, better understanding of optimal transfer strategies based on coherent and incoherent transfer in the hypothetical model systems may serve as a stepping stone for improved experiments with more realistic relaxation rates and a larger number of spins. Optimal control based methods make it possible to study the effect of experimental imperfections and constraints such as maximum MW and RF amplitudes, minimal switching times of arbitrary waveform generators, resonator bandwidth etc., which may motivate the development of new spectrometer hardware with improved DNP performance. In addition to the study of optimal incoherent and coherent electron-nuclear polarization transfer, the optimal control based GRAPE algorithm can also be used for the optimization of decoupling sequences **[93]** with potential applications in electron-nuclear spin systems.

5. **Discussion**

5.1. *Comparison with Theoretical Models*

DNP measurements of nitroxide radicals (TEMPOL or TEMPONE) dissolved in water have been carried out over a very large magnetic field range from 10 mT up to 10 T (Table 4). For the first time, this allows to follow the DNP enhancement dispersion curve from very low magnetic fields, where the theoretical predictions for proton spins are 330, up to such high magnetic fields where very small DNP enhancements are predicted. The experimental DNP enhancements can be compared quantitatively with coupling factors, which are calculated by the classical SBM and force-free diffusion models (see section 4.3) or extracted from MD trajectories **[64]**, because many other spin parameters, like electron and nuclear spin relaxation and electron spin saturation have been determined independently. Figure 24 summarizes on a double-logarithmic scale the experimental DNP results obtained in Berlin, Frankfurt, Göttingen and Karlsruhe (black dots). The maximum achievable DNP enhancements (assuming both a saturation and leakage factor of 1) from the theoretical SBM and force-free models (in yellow) and from MD calculations (in red) are shown for temperatures ranging from 25 to 45°C in the same plot for comparison. For the SBM and force-free model calculations, the translational and rotational correlation times have been taken from NMRD measurements **[35, 52]**.

Before comparing the experimental DNP enhancements with the theoretical and computational models, it is important to stress again the experimental difficulties and limitations of this diagram. First of all, every data point corresponds to a different experimental setup; resulting in different sample sizes, available microwave power, microwave resonant structures and therefore different overall performance. In all cases, a full saturation of the electron spin transition was not achieved. The reason for that is related to the nitroxide radicals used, as well as the water solvent. The large hyperfine splitting of the EPR line by the nitrogen coupling (about 60 MHz for ^{15}N) would require very high microwave field strength to fully saturate both hyperfine lines simultaneously, as explained above. On the other hand the strong microwave absorption of liquid water limits the maintainable microwave power to prohibit excessive heating of the sample. Additionally, for most of the microwave resonant structures used, the microwave B_1 field is not homogeneous over the sample size, resulting in reduced average saturation factors for the NMR signal integrated over the whole sample. For this reason, all experimental DNP enhancement data points are expected to fall below the theoretical predictions, which assume total saturation and a leakage factor of 1. This is indeed the case for the DNP measurements at very low magnetic fields. The two data points below 0.1 T show the same DNP enhancement, corresponding to a full saturation of only a single hyperfine line of TEMPOL, both for ^{14}N and ^{15}N. At 0.3 T, where ELDOR measurements allowed an independent estimation of the saturation factor to $s = 0.9$ **[33]**, the agreement between theoretical predictions and experimental results is excellent, once these independently determined factors *s* and *f* are considered. Beyond the magnetic field of 0.1 T the DNP enhancements start to drop, experimentally as well as theoretically, for this specific agent/target system. Nevertheless, the experimentally observed enhancements still amounts to $\varepsilon =$ -19 at a magnetic field of 9.4 T. Interestingly, the slope of the experimentally observed DNP enhancement seems to be less steep compared to the classical models (which are derived under the assumption of rigid molecules) and is better represented by the MD calculations. The big change of the predicted DNP enhancements as a function of the temperature, as seen in the force-free model, arises from its non-linear dependence on the translational correlation in this regime. This time changes from 26 to 11 ps by changing the temperature from 20°C to 55°C respectively, as extracted from NMRD data.

In conclusion, the SBM and force-free diffusion models describe very well the experimental data below 2 T; however, the experimental enhancements at higher magnetic fields seem to decay slower than predicted from these models. This is indeed not very surprising since these models assume that the molecules move rigidly during their rotational and translational diffusion. This assumption is satisfactory at low fields, but not at high fields. In fact, the presence of dynamics on a much shorter timescale, resulting from local motions in the radical-target complex, plays an important role in determining the coupling factor above 2 T, because the zero quantum and double quantum spectral density functions related to the global rotational and translational correlation times are almost completely dispersed. Therefore, the spectral density functions describing the nuclear relaxation should be evaluated taking into account the presence of these fast motions. This could be done by introducing the correlation times of the fast motions in the SBM and diffusion models, using a model-free approach **[94]**, or through system-specific MD calculations. Indeed, the MD simulations performed for TEMPONE indicate such faster processes to occur, and therefore predict a less dramatic decrease of the enhancement as shown in figure 15 **[64]**. The experimental data points at high field are as high as the MD predicted maximum DNP enhancement (for full saturation and a leakage factor of 1), despite the fact that both *s* and *f* are without doubt below 1. That might be explained by the elevated temperature of the samples above 45°C. Overall the agreement between the MD simulations and the experimental DNP enhancements seems very good, taking into account all experimental uncertainties.

In this context, experimental results obtained from other laboratories are also very interesting and insightful and should be discussed. The Warwick group obtained similar enhancements at a magnetic field of 3.4 T for TEMPOL in water as reported here **[95]**, additionally they observed very high enhancements of up to 50 for TEMPOL in toluene **[96]**. The group in Nijmegen obtained even higher enhancement factors of up to 65 for TEMPOL dissolved in water, again at a magnetic field strength of 3.4 T **[97]** and calculated from their known microwave field profile a maximum experimental enhancement of 94. This value would clearly exceed the predictions from MD calculations, but unfortunately the real sample temperature could not be determined for this measurement. Our own measurements performed at 9.4 T with Fremy's salt in liquid water solution gave the highest DNP enhancements at this field (see Table 4). Indeed, also MD calculations predict a 1.6 times larger coupling factor compared to TEMPONE for this radical-solvent pair.

In summary, the absolute value of the coupling factor predicted from MD simulations seems to be somewhat too low to fully explain the observed experimental enhancements. More sophisticated quantum-chemical dynamic simulations which include the time-dynamics of the unpaired electron spin density and are able to describe sub-ps timescales of the DNP agent-target pair might further improve the agreement between such predictions and experimental DNP enhancements at high fields. Potentially such calculations could help to further optimize the radical-target system for DNP applications at high magnetic fields. Indeed, the overall picture emerging from experiments and simulations is that high field DNP is much more promising than we thought only a few years ago, and this awareness should stimulate further research and investments.

5.2.Optimum Polarizing Field for Liquid DNP

Two limiting cases will be considered to find the optimum polarizing field for liquid DNP:

a) very small (size limited) or dielectric lossless samples

b) large samples with strong microwave absorption

In case a) the optimum DNP enhancement for NMR detection at high magnetic fields will be obtained at highest polarizing field. That holds at least up to 10 T / 400 MHz proton frequency as can be seen from the experimental achieved DNP enhancements at different magnetic fields.

With the technical and instrumental problems described above the situation becomes more complex in case b). The frequency dependence of the microwave absorption, which determines the effective sample volume, as well as the frequency dependence of the DNP enhancement has to be taken into account to predict an optimum polarization field. A merit function $M(B_0)$ can be defined, which takes all these factors into account. For volume samples with standard NMR detection this is given by:

$$M = \varepsilon \cdot (B_{pol}/B_{det}) \cdot (V_{DNP}/V_{NMR}) \qquad (13)$$

where ε is the DNP enhancement, B_{pol} and B_{det} are the polarizing and detection fields, V_{DNP} and V_{NMR} are the respective sample volumes for DNP and standard NMR. Microwave resonance structures have to be used to minimize the microwave heating of the sample, as explained above. Two different structures can be used: fundamental mode resonators, where the sample volume scales with $V_{DNP} \sim 1/ B_{pol}^3$, or resonance structures, which are extended in two dimensions and are only restricted in one dimension by the microwave wavelength (see below). For such structures the sample volume scales with $V_{DNP} \sim 1/ B_{pol}$. The dimensions in the other two directions are only limited by the area of the homogeneous magnetic field. Approximating the frequency dependence of the DNP enhancement by $\varepsilon \sim 1/ B_{pol}$, this leads to a decrease of the merit function $M \sim 1/ B_{pol}^n$ by increasing the magnetic field, where n ranges from 1 to 3. Therefore, the maximum value for M will be achieved at the maximum polarization field where optimum polarization is still achieved (see Figure 2 and Figure 24).

For small radicals in non-viscous solvents this will be approximately at 0.3 T (corresponding to X-band frequencies). With a maximum achievable polarization of -330 (for dipolar coupling) this would give an effective DNP enhancement of -5 at the highest momentarily available detection field of 25 T (1 GHz NMR frequency).

Unfortunately, even at such microwave frequencies, the typical sample volume have to be reduced compared to standard NMR samples to avoid excessive microwave heating (about a factor of 10 for water).

The frequency dependence of the permittivity $\varepsilon=\varepsilon'+i\varepsilon''$ can be used to estimate this sample volume reduction. For samples in 2D overmoded resonators with height z, the percentage of microwave power absorbed will be given by:

$$(P_0-P(z))/P_0=1-exp(-\delta k \cdot z)=1-exp(-\delta \omega_{MW} \cdot \sqrt{(\mu\varepsilon')} \cdot z) \approx \delta \omega_{MW} \cdot \sqrt{(\mu\varepsilon')} \cdot z \qquad (14)$$

with the microwave loss tangent δ defined by $tan\delta=\varepsilon''/\varepsilon'$.

For a comparable microwave performance of the resonator the left side of this equation has to be kept constant, thus the relative size of the sample V_{DNP} as a function of the microwave frequency can be predicted if the permittivity ε is known:

$$V_{DNP} \sim c / \omega_{MW} \qquad (15)$$

where $c^{-1} = \delta \cdot \sqrt{(\mu\varepsilon')}$ is solely defined by the permittivity ε of the solvent. For water ε has a strong nonlinear frequency dependence leading to a strong frequency dependence of the factor c (Tab. 7):

A polarization field somewhat lower than X-band might be advantageous for liquid water samples if large sample volumes are required (see Table 7). Other experimental and sample parameters, like available microwave power and field dependence of the relaxation rates, might further complicate this optimization.

5.3. Strategies for Liquid DNP Spectrometers

In conclusion, both described strategies - direct polarization at the high magnetic field of NMR detection (HF-DNP) and polarization at a low magnetic field with subsequent fast shuttling of the sample to the high magnetic field for NMR detection (shuttle-DNP) - have their specific advantages and limitations.

For the shuttle DNP approach, higher absolute signal enhancements are expected for non size-restricted samples. The field profile between polarizing and detection field is crucial to avoid polarization losses within the shuttle time, especially for macromolecules. Therefore, a single-bore two center magnet system is required. Due to the possibility of reliable repeating the experiment, this approach might be very useful in the future for DNP signal enhancement in multidimensional NMR studies on macromolecules. Additionally, it might be possible to use higher polarized non-Boltzmann electron spin systems (as for example optical excited triplet states or radical pairs) to overcome the penalty of polarizing at low magnetic fields.

With the HF-DNP setup unexpected large DNP enhancements have been observed up to fields of 10 T. On the other hand, the sample size had to be decreased dramatically to avoid microwave heating of the sample. Therefore, with fundamental mode resonators, net signal enhancement can be only expected for size limited microscopic samples. More elaborate resonance structures, as described above, could potentially increase the sample volume up to a few µl and achieve higher NMR conversion factor as well. Such 2D-overmoded extended structures need higher microwave excitation power levels of several W to saturate the electronic transitions of typically used nitroxide radicals. Therefore a gyrotron microwave source will be crucial for such new probes.

Thus, if the technical problems related to sample size, heating by the electrical field and homogeneity of the magnetic field can be solved, HF-DNP might also be useful for sensitivity improvements on medium sample volumes. The possibility of exciting and detecting electron and nuclear spins simultaneously without any time delays and without physical movement of the sample is unique for this approach and offers versatile prospects for coherent spin manipulations, which might lead to improved polarization transfer pathways and new types of experiments.

Pulsed microwave excitation with inter-pulse spacing similar to T_{1e} of the radical might allow doubling the achieved enhancement for both methods. More advanced pulsing schemes utilizing coherent pathways could increase the enhancement further, as has been discussed. Technically, the implementation of advanced pulsing schemes should be much easier accomplished at X-band frequencies compared to very high microwave frequencies above 100 GHz, but in principle commercial pulse EPR spectrometer exist up to 260 GHz frequencies.

6. **Conclusions and Outlook**

For the first time DNP spectrometer for high-field liquid NMR studies have been successfully constructed and used to experimentally probe the maximum obtainable DNP enhancement at high magnetic fields. Substantial DNP enhancements of the NMR signals have been observed for the HF-DNP as well as the Shuttle-DNP approach. HF-DNP at 9.4 T can reach substantial DNP enhancements (> 20). For size restricted samples, or non-polar solvents, this offers a large increase in sensitivity. Further efforts in cavity design have to be undertaken to make this approach applicable for biomolecular studies. Shuttle DNP is annother promising technique for the general enhancement of NMR signals of molecules in aqueous solution. The overall enhancements are somewhat lower in this approach (<10), but larger sample volumes and high spectral resolution are easier achieved with this method. With the enhancement achieved on glucose, applications for unfolded and globular proteins are within reach. In both cases, the experiments can be repeated fast, making it promising techniques for general multi-dimensional applications.

First experiments with model compounds open, on the one hand, the grounds for a thorough theoretical analysis of the physical principles of the polarization transfer mechanism and allow, on the other hand, optimization of the experimental setups. In combination with the performed NMR relaxation dispersion experiments and pulsed EPR investigation of the radical relaxation properties, benchmark data have been created for further investigations. Under optimized experimental conditions significant NMR signal enhancements can be predicted in liquids. Nevertheless, much further work has to be performed to explore the full potential of the method.

6.1. *Other Polarization Agents*

The Boltzmann penalty of the shuttle-DNP approach, which arises by the thermal electron spin polarization at the lower magnetic field, might be overcome by photo-generated radical spin states as DNP polarizing agents. It is known from photo-excited radical pair or triplet states that such electron spin systems can have a spin polarization or spin alignment close to unity, which would drastically increase the starting polarization. The electron spin polarization has to exist long enough for a coherent manipulation of the spin system; for X-band frequencies such manipulations can nowadays be done on the ns-time scale for the electron spin system.

Transition metal ions or complexes also represent an interesting class of DNP agents for applications in structural biology or in catalysis. Unfortunately, most metal cofactors in metalloproteins have very fast electronic relaxation rates and broad EPR spectra at room temperature. Therefore, the best candidates must be identified for attempting DNP experiments according to their electron relaxation properties, which can be determined either by EPR spectroscopy or NMRD measurements. Besides the nature of the metal ion, the electron relaxation rates depend on the molecular geometry and on the nature of the chelating group. In most cases, the presence of low-lying excited states, which make spin-orbit coupling more efficient, determines the electronic spin relaxation field and its temperature dependence **[34]**. For low lying excited states with energies comparable with $k_B \cdot T$, T_{1e} values are typically shorter than 10^{-11} s (like titanium(III), with $T_{1e} \approx 10^{-11}$ s, low spin iron(III), with $T_{1e} \approx 10^{-11}$ to 10^{-12} s, high spin cobalt(II), high spin iron(II), lanthanides(III) except gadolinium(III), with $T_{1e} \approx 10^{-12}$ s), and therefore not suitable for electron spin saturation and DNP experiments. Metal ions with an electron spin quantum number equal to ½ (i.e. without ZFS) relax due to modulation of the anisotropy in the hyperfine coupling to the metal nucleus and/or of the g tensor, when the orbitally non-degenerate ground state is well separated by excited states. Among them there are copper(II) and oxovanadium (IV) complexes. The electronic relaxation times are relatively long (10^{-8}-10^{-10} s at room temperature), without any field dependence. The ^{1}H NMRD profiles of copper proteins actually indicated electron relaxation rates of few nanoseconds, i.e. large enough to be considered for DNP applications. In S>1/2 systems with a non-degenerate ground state, small transient ZFS (Δ_t) is always present. Typical examples are manganese(II), high spin iron(III), chromium(III), nickel(II) in O_h symmetry, and gadolinium(III). The most efficient electron relaxation mechanism in these cases is due to the modulation of transient ZFS. Such modulation is ascribed to the correlation time for the collisions of the solvent molecules, responsible for the deformation of the coordination polyhedron. This relaxation mechanism makes the electron relaxation rate field dependent. Typical values for the electron relaxation rates at low fields are $T_{1e}\approx 10^{-9}$-10^{-11} s, but they can increase by orders of magnitude at 400-600 MHz, thus becoming more promising for high field DNP applications **[98]**, although T_{2e} values do not increase analogously. In complexes where a static ZFS is also present, modulation of this ZFS with a correlation time related to the reorientation time of the complex is a possible further electron relaxation mechanism. This is the case with several manganese(II) proteins and more importantly with iron(III) compounds. The magnitude of transient ZFS is here expected to be related to that of the static ZFS; the former can be seen as a perturbation of the latter. As a consequence, systems with increasing static ZFS experience faster electron relaxation rates. Figure 25 shows the water ^{1}H nuclear magnetic relaxation dispersion (NMRD) curves for a solution of Mn^{2+} concanavalin

A. From the field dependence of the relaxation rates, the electron relaxation parameters were obtained, and T_{1e} and T_{2e} values of 5 μs and 1 ns, respectively, could be estimated for 400 MHz of proton Larmor frequency (9.4 T magnetic field). With efficient microwave resonant structures and high power microwave sources, partial electron spin saturation could be achieved under such conditions.

6.2. Higher Magnetic Fields

It is rather difficult to predict DNP performance at even higher magnetic fields up to 28 T. If indeed local librational dynamic modes are important for the Overhauser DNP mechanism at high magnetic fields, the efficiency might even become better again by coupling for example to H-bonding librations of the agent-target complex. For shuttle-DNP the Boltzmann penalty will reduce the enhancement, thus the excitation field would have to be shifted to higher magnetic fields respectively. Technical problems of microwave excitation, transmission and sample size are also becoming more severe at higher frequencies. At the highest possible magnetic fields available for NMR spectroscopy already THz optical and far-infrared technology might be used for the excitation of the electronic spin system, leading to another technology switch.

6.3. *Potential Application Areas*

Application to size restricted samples can be most easily foreseen. This could be of interest for the field of analytical chemistry, where NMR could be directly coupled to HPLC, electrophoresis and mass-spectrometry. Other applications could be in the field of micro-fluidity, biofluids or micro-reaction chambers to follow fast chemical reactions. Shuttle-DNP could be applied to biomolecular structure investigations, gaining another factor of about 3 in sensitivity. Additionally, DNP enhancements could be used to obtain selectivity and specificity, for example by covalently attached spinlabels. In addition to the possibility to enhance the NMR sensitivity, these new tools will also allow to address other questions. HF-DNP might be a very good tool to study accessibility (for example to catalytic sites or binding pockets) and diffusive processes (for example in micro-pores, protein channels or through membranes), because of the extreme sensitivity of the DNP effect at high magnetic fields to fast local motions. Regardless of the technical problems, which still have to be overcome and solved, interesting scientific applications have already started.

Acknowledgments

This project was funded by the European Design Study Project: Dynamic Nuclear Polarization for Liquid State NMR in Structural Biology. M. Prandolini, M. Gafurov, B. Endeward, S. Lyubenova, J. Krummenacker and D. Sezer are thanked for their contribution to the scientific work in Frankfurt. M.T. Türke and I.Tkach for their contributions in the 9 and 94 GHz DNP work in Göttingen. Thorsten Marquardsen, Alexander Krahn, and Andreas Tavernier at Bruker for the work on the hardware. Nikolas Pomplun (Munich) is thanked for his contributions to the calculation of coherent transfer efficiencies. The work at FU Berlin would not have been possible without the contributions by Konstantin Ivanov, Yuri Grishin, Alexey Kiryutin, Talea Köchling, Sergey Korchak, Karsten Miesel, Alexandra Yurkovskaya and Herbert Zimmermann.

B. Endeward, D. Schütz, J. Krummenacker, I. Krstic, P. Neugebauer and L. Prisner are thanked for proof-reading of the manuscript.

We would like to acknowledge the other coworkers within the EU project: R. Boolens (Utrecht), N. Nielsen (Aarhus), G. Smith (St. Andrews), P. Tordo (Marseille). I. Solovyeva and C. Börner are thanked for their helpful contribution to the management of the project. Special thanks go to the associated member of this Design Study from U.S.A., Prof. R. G. Griffin (Cambridge) for many fruitful discussions.

References

[1] R.R. Ernst, G. Bodenhausen and A. Wokaun, *Principles of Nuclear Magnetic Resonance in One and Two Dimensions*, Clarendon Press, Oxford (1987).

[2] A.W. Overhauser, Phys. Rev. 92, (1953) 411-415.

[3] T.R. Carver and C.P. Slichter, Phys. Rev. 92, (1953) 212-213.

[4] H.G. Beljers, L. van der Kint and J.S. van Wieringen, Phys. Rev. 95, (1954) 1683.

[5] K.H. Hausser and D. Stehlik, Adv. Magn. Reson. 3, (1968) 79-139.

[6] W. Müller-Warmuth and K. Meise-Gresch, Adv. Magn. Reson. 11, (1983) 1-45.

[7] C.D. Jeffries, Phys. Rev. 106, (1957) 164—165.

[8] A. Abragam, J. Combrisson and I. Solomon, C. R. Acad. Sci. 247, (1958) 2337-2340.

[9] A.V. Kessenikh, V.I. Lushchikov, A.A. Manenkov and Y.V. Taran, Sov. Phys. Solid State 5, (1963) 321-329.

[10] A.V. Kessenikh, A.A. Manenkov and G.I. Pyatnitskii, Sov. Phys. Solid State 6, (1964) 641-643.

[11] C.F. Hwang and D.A. Hill, Phys. Rev. Lett. 18, (1967) 110-112.

[12] C.F. Hwang and D.A. Hill, Phys. Rev. Lett. 19, (1967) 1011-1014.

[13] B.N. Provotorov, Soviet Phys. JETP 14, (1962) 1126-1131.

[14] M. Borghini, Phys. Rev. Lett. 20, (1968) 419-421.

[15] M. Goldman, *Spin Temperature and Nuclear Magnetic Resonance in Solids*, Oxford University Press, Oxford (1970).

[16] R.A. Wind, M.J. Duijvestijn, C. van der Lugt, A. Manenschijn and J. Vriend, Prog. NMR Spectr. 17, (1985) 33-67.

[17] D.J. Singel, H. Seidel, R.D. Kendrick and C.S. Yannoni, J. Magn. Reson. 81, (1989) 145-161.

[18] M. Afeworki, R.A. McKay and J. Schaefer, Macromolecules 25, (1992) 4084-4091.

[19] V. Weis, M. Bennati, M. Rosay, J.A. Bryant and R.G. Griffin, J. Magn. Reson. 140, (1999) 293-299.

[20] T. Maly, G.T. Debelouchina, V.S. Bajaj, K.-N. Hu, C.-G. Joo, M.L. Mak-Jurkauskas, J.R. Sirigiri, P.C.A. van der Wel, J. Herzfeld, R.J. Temkin and R.G. Griffin, J. Chem. Phys. 128, (2008) 052211.

[21] K.-N. Hu, H.-hua Yu, T.M. Swager and R.G. Griffin, J. Am. Chem. Soc. 126, (2004) 10844-10845.

[22] V.S. Bajaj, C.T. Farrar, M.K. Hornstein, I. Mastovsky, J. Vieregg, J. Bryant, B. Eléna, K.E. Kreischer, R.J. Temkin and R.G. Griffin, J. Magn. Reson. 160, (2003) 85-90.

[23] J.H. Ardenkjaer-Larsen, B. Fridlund, A. Gram, G. Hansson, L. Hansson, M.H. Lerche, R. Servin, M. Thaning and K. Golman, Proc. Natl. Acad. Sci. U.S.A. 100, (2003) 10158-10163.

[24] K. Golman, R. in't Zandt, M. Lerche, R. Pehrson and J.H. Ardenkjaer-Larson, Cancer Res. 66, (2006) 10855-10860.

[25] R. A. Dwek, H. D. W. Hill, J. G. Kenworthy, D. F. S. Natusch, R. E. Richards, Mol. Phys. 13, (1967) 27-36.

[26] I. Solomon, Phys. Rev. 99, (1955) 559-565.

[27] A. Abragam, *Principles of Nuclear Magnetism*, Oxford University Press, Oxford, (1961).

[28] J. S. Hyde, J. C. W. Chen and J. H. Freed, J. Chem. Phys., 48, (1968) 4211-4226.

[29] R.D. Bates and W.S. Drozdoski, J. Chem. Phys. 67, (1977) 4038-4044.

[30] B.H. Robinson, D.A. Haas and C. Mailer, Science 263, (1994) 490-493.

[31] B.D. Armstrong and S. Han, J. Chem. Phys. 127, (2007) 104508.

[32] D. Sezer, M. Gafurov, M.J. Prandolini, V.P. Denysenkov and T.F. Prisner, Phys. Chem. Chem. Phys. 11, (2009) 6638-6653.

[33] M. T. Türke and M. Bennati, Phys. Chem. Chem. Phys. 13, (2011) 3630–3633.

[34] I. Bertini, C. Luchinat, G. Parigi, Adv. Inorg. Chem. 57, (2005) 105-172.

[35] M. Bennati, C. Luchinat, G. Parigi and M.-T. Türke, Phys. Chem. Chem. Phys. 12, (2010) 5902-5910.

[36] A. Abragam and R. V. Pound, Phys. Rev. 92, (1953) 943-962.

[37] L.-P. Hwang and J. H. Freed, J. Chem. Phys., 63, (1975) 4017.

[38] I. Bertini, C. Luchinat and G. Parigi, *Solution NMR of Paramagnetic Molecules*, Elsevier Press, Amsterdam (2001).

[39] H.C. Dorn, R. Gitti, K.H. Tsai and T.E. Glass, Chem. Phys. Lett. 155, (1989) 227-232.

[40] B.D. Armstrong, M.D. Lingwood, E.R. McCarney, E.R. Brown, P.Blümler and S. Han, J. Magn. Reson. 191, (2008) 273-281.

[41] K. Münnemann, C. Bauer, J. Schmiedeskamp, H.W. Spiess, W.G. Schreiber and D. Hinderberger, Appl. Magn. Reson. 34, (2008) 321-330.

[42] M. Reese, M.-T. Türke, I. Tkach, G. Parigi, C. Luchinat, T. Marquardsen, A. Tavernier, P. Höfer, F. Engelke, C. Griesinger and M. Bennati, J. Am. Chem. Soc. 131, (2009) 15086-15087.

[43] A. Krahn, P. Lottmann, T. Marquardsen, A. Tavernier, M.-T. Türke, M. Reese, A. Leonov, M. Bennati, P. Hoefer, F. Engelke and C. Griesinger, Phys. Chem. Chem. Phys. 12, (2010) 5830-5840.

[44] K. Miesel, K.L. Ivanov, T. Köchling, A.V. Yurkovskaya and H.-M. Vieth, Appl. Magn. Reson. 34, (2008) 423-437.

[45] C. Luchinat, G. Parigi, Appl. Magn. Reson. 34, (2008) 379-392.

[46] M. Reese, D. Lennartz, T. Marquardsen, P. Höfer, A. Tavernier, P. Carl, T. Schippmann, M. Bennati, T. Carlomagno, F. Engelke, C. Griesinger, Appl. Magn. Reson. 34, (2008) 301-311.

[47] Y.E. Nesmelov, A. Gopinath, D.D. Thomas, J. Magn. Reson. 167, (2004) 138–146

[48] V.P. Denysenkov, M.J. Prandolini, A. Krahn, M. Gafurov, B. Endeward and T.F. Prisner, Appl. Magn. Reson. 34, (2008) 289-299.

[49] F. Engelke, Concepts Magn. Reson. 15, (2002) 129-155.

[50] V. Denysenkov, T. Prisner, J. Stubbe, M. Bennati, Appl. Magn. Reson. 29, (2005) 375-384.

[51] M. Hertel, V. Denysenkov, M. Bennati, T. Prisner, Magn. Reson. Chem. 43, (2005) 248–255.

[52] P. Höfer, G. Parigi, C. Luchinat, P. Carl, G. Guthausen, M. Reese, T. Carlomagno, C. Griesinger and M. Bennati, J. Am. Chem. Soc. 130, (2008) 3254-3255.

[53] M. T. Türke, I. Tkach, M. Reese, P. Höfer and M. Bennati, Phys. Chem. Chem. Phys. 12, (2010) 5893-5901.

[54] C. Luchinat, G. Parigi, J. Am. Chem. Soc. 129, (2007) 1055-1064.

[55] S. Korchak, K. Ivanov, A. Yurkovskaya and H.-M. Vieth, J. Chem. Phys. 133, (2010) 194502.

[56] W. L. Hubbell, D. S. Cafiso and C. Altenbach, Nat. Struct. Biol. 7, (2000) 735–739.

[57] A. D. Milov, A. B. Ponomarev, Y. D. Tsvetkov, Chem. Phys. Lett. 110, (1984) 67-72.

[58] O. Schiemann and T. F. Prisner, Quart. Rev. Biophys. 40, (2007) 1-53.

[59] G. M. Clore, Mol. BioSys. 4, (2008) 1058-1069.

[60] C. S. Klug and J. B. Feix, Methods in Cell Biology, 84 (2008) 617-658.

[61] R. A. Wind and J. H. Ardenkjaer-Larsen, J. Magn. Reson. 141, (1999) 347-354.

[62] M.J. Prandolini, V.P. Denysenkov, M. Gafurov, B. Endeward and T.F. Prisner, J. Am. Chem. Soc. 131, (2009) 6090-6092.

[63] J. Kowalewski, D. Kruk, G. Parigi, Adv. Inorg. Chem. 57, (2005) 41-104.

[64] D. Sezer, M.J. Prandolini and T.F. Prisner, Phys. Chem. Chem. Phys. 11, (2009) 6626-6637.

[65] M. Carravetta, O.G. Johannessen, M.H. Levitt, Phys Rev Lett, 92 (2004) 153003.

[66] F.J.J. De Kanter and R. Kaptein, Chem. Phys. Lett., 62 (1979) 421-426.

[67] K. L. Ivanov, A. V. Yurkovskaya, H.-M. Vieth, J. Chem. Phys. 128, (2008) 154701.

[68] K. L. Ivanov, A. V. Yurkovskaya, H.-M. Vieth, J. Chem. Phys. 129, (2008) 234513.

[69] A. Kiryutin, K. Ivanov, A. Yurkovskaya, H.-M. Vieth, Sol. State Nuc. Mag. Reson., 34 (2008) 142-149.

[70] I. Bertini, Y.K. Gupta, C. Luchinat, G. Parigi, C. Schlörb, H. Schwalbe, Angew. Chem. Int. Ed. 44, (2005) 2223-2225.

[71] V. Borsi, C. Luchinat, G. Parigi, Biophys. J. 97, (2009) 1765-1771.

[72] S. E. Korchak, A. S. Kiryutin , K. L. Ivanov , A. V. Yurkovskaya , Yu. A. Grishin , H. Zimmermann , H.-M. Vieth, Appl. Magn. Reson. 37, (2010) 515–537.

[73] S. Un, T. Prisner, R.T. Weber, M.J. Seaman, K.W. Fishbein, A.E. McDermott, D.J. Singel and R.G. Griffin, Chem. Phys. Lett. 189, (1992) 54-59.

[74] S.R. Hartmann and E.L. Hahn, Phys. Rev. 128, (1962) 2042-2053.

[75] H. Brunner, R.H. Fritsch and K.H. Hausser, Z. Naturforsch. A 42, (1987) 1456-1457.

[76] A. Henstra, P. Dirksen, J. Schmidt and W. Th. Wenckebach, J. Magn. Reson. 77, (1988) 389-393.

[77] A. Henstra and W.Th. Wenckebach, Mol. Phys. 106, (2008) 859-871.

[78] A. Henstra, P. Dirksen and W.Th. Wenckebach, Phys. Lett. A 134, (1988) 134-136.

[79] A. Henstra, T.-S. Lin, J. Schmidt and W.Th. Wenckebach, Chem. Phys. Lett. 165, (1990) 6-10.

[80] N. Bleombergen and P. P. Sorokin, Phys. Rev. 110, (1958) 865-875.

[81] R.A. Wind, L. Li, H. Lock and G.E. Maciel, J. Magn. Reson. 79, (1988) 577-582.

[82] R.A. Wind and H. Lock, Adv. Magn. Opt. Reson. 15, (1990) 51-77.

[83] C.T. Farrar, D.A. Hall, G.J. Gerfen, M. Rosay, J.-H. Ardenkjaer-Larsen and R.G. Griffin, J. Magn. Reson. 144, (2000) 134-141.

[84] V. Weis, M. Bennati, M. Rosay and R.G. Griffin, J. Chem. Phys. 113, (2000) 6795-6802.

[85] V. Weis and R.G. Griffin, Solid State Nucl. Magn. Reson. 29, (2006) 105-117.

[86] N. Pomplun, B. Heitmann, N. Khaneja and S.J. Glaser, Appl. Magn. Reson. 34, (2008) 331-346.

[87] N. Khaneja, T. Reiss, C. Kehlet, T. Schulte-Herbrüggen, S.J. Glaser, J. Magn. Reson. 172, (2005) 296-305.

[88] Z. Tosner, T. Vosegaard, C. T. Kehlet, N. Khaneja, S. J. Glaser, N. C. Nielsen, J. Magn. Reson. 197, (2009) 120-134.

[89] T. O. Reiss, N. Khaneja, S.J. Glaser, J. Magn. Reson. 154, (2002) 192-195.

[90] N. Khaneja, F. Kramer, S.J. Glaser, J. Magn. Reson. 173, (2005) 116-124.

[91] R.A. Craig, R.K. Harris, R.J. Morrow, Org. Magn. Reson. 13, (1980) 229-231.

[92] N. Pomplun and S. J. Glaser, Phys. Chem. Chem. Phys. 12, (2010) 5791-5798.

[93] J. L. Neves, B. Heitmann, N. Khaneja, S. J. Glaser, J. Magn. Reson. 201, (2009) 7-17.

[94] G. Lipari, A. Szabo, J. Am. Chem. Soc. 104, (1982) 4546-4559.

[95] E. V. Kryukov, K. J. Pike, T. K. Y. Tam, M. E. Newton, M. E. Smith, R. Dupree, Phys. Chem. Chem. Phys. 13, (2011) 4372-4380.

[96] E. V. Kryukov, M. E. Newton, K. J. Pike, D. R. Bolton, R. M. Kowalczyk, A. P. Howes, M. E. Smith, R. Dupree, Phys. Chem. Chem. Phys. 12, (2010) 5757-5765.

[97] J. A. Villanueva-Garibay, G. Annino, P. J. M. Van Bentum, A. P. M. Kentgens, Phys. Chem. Chem. Phys. 12, (2010) 5846-5849.

[98] B. Corzilius, A.A. Smith, A.B. Barnes, C. Luchinat, I. Bertini, R.G. Griffin, J. Am. Chem. Soc., 133, (2011) 5648-5651.

Tables:

Lower field (DNP) position	0.34 T
High field (NMR) position	14 T
Shuttle time (low-high field)	40 ms
Microwave frequency	9.4-9.7 GHz
Microwave power (CW / Pulsed)	5 / 20 W
MW cavity Q factor	1725
MW cavity conversion factor	0.55 mT/W$^{1/2}$
Microwave transmission losses	1.5 dB
Sample size	6 µl

Table 1: Specifications of Sample Shuttle Spectrometer

Lowest magnetic field	50 µT
Highest magnetic field	7 T
Minimum shuttle time	0.29 s
NMR linewidth	< 0.3 Hz
EPR excitation frequencies	75 MHz, 300 MHz, 1.4 GHz
MW pulse length	5 ns – 25 µs
MW pulse power	100 W @ 300 MHz, 40 W @ 1.4 GHz
B_1 microwave field strength at sample	0.85 mT @300MHz and 75 MHz, 0.1 mT @ 1.4 GHz
Sample size	0.3 ml

Table 2: Specification of the Probe Shuttle DNP spectrometer

Magnetic field	9.4 T
Magnetic field sweep range	80 mT
MW sweep range (solid state source)	257.5- 259.5 GHz
Microwave power (solid state source / gyrotron)	40 mW / 20 W

MW transmission losses	1.8 dB
MW cavity Q factor (empty)	650
MW B_1 conversion factor	0.27 $mT/\sqrt{W}$
RF B_2 conversion factor	0.64 $mT/\sqrt{W}$
Sample size	5 nl

Table 3: Specifications of the High-field DNP Setup

EPR frequency [GHz]	DNP enhancement E	Sample	MW power [W]
0.3	-110 / -165	^{14}N / ^{15}N TEMPOL 25 mM	40
1.4	-110 /-165	^{14}N / ^{15}N TEMPOL 25 mM	40
9.5	-190	^{15}N-TEMPONE 25 mM	20
95	-43	^{15}N-^{2}H-TEMPONE, 25 mM	0.4
260	-30	^{15}N-Fremy Salt, 75 mM, 27°C	0.6
260	-28	^{15}N-TEMPOL 40 mM, 70°C	0.3

Tab.4: Experimental Measured DNP Enhancements of Liquid Nitroxide/Water Solutions at various Fields.

Region [ppm]		ε^{HF}
4.80 – 4.40	H_2O	-3.2
3.60 – 3.50	$\underline{CH_3}$-CH_2-OH	-1.6
1.15 – 1.05	CH_3-$\underline{CH_2}$-OH	-1.8
-0.05 – -0.10	DSS	-1.2

Table 5: Shuttle DNP Parameters on Ethanol. Measured enhancement factors of Figure 19 with t_p = 12 ns and the spin lattice relaxation time T_1 of the low and high field position for a sample of 5 mM perdeuterated TEMPONE-^{15}N solution (80/20 H_2O/D_2O) with 10 mM DDS and 0.1 M ethanol

Region [ppm]	Groups	ε^{HF}
5.30 - 5.00	D – glycopyranose 1α	-2.2
4.60 - 4.50	D – glycopyranose 1β	-2.8
5.00 - 4.10	H_2O	-3.7
3.90 - 3.55	D – glycopyranose 3α + 5α + 6α + 6β	-1.4
3.50 - 3.10	D – glycopyranose 2α + 4α + 2β+ 3β+4β + 5β	-1.5
0.10 - -0.30	DSS	-2.0

Table 6: Shuttle DNP Parameters of Glucose. Enhancement factors as determined from the integral values of the selected signal regions in Figure 20.

Frequency [GHz]	1	10	40	100	300
Factor c	8.5	1	0.9	1.4	1.9

Tab. 7: Frequency Dependence Correction Factor. Correction factor for sample volumes at different frequencies given by the frequency dependence of ε

Figure Captions:

Figure 1: Energy level diagram for an electron spin S=1/2 coupled to a nuclear spin I=1/2. W_I: nuclear spin relaxation rate, W_S: electron spin relaxation rate, W_2: double quantum relaxation rate, W_0: zero quantum relaxation rate.

Figure 2: Field dependence of coupling factor. The coupling factor ξ is shown as a function of the external magnetic field B_0 for rotational (solid line) or translational (dotted line) motions with a correlation time τ_c of 20 ps.

Figure 3: Two-center shuttle DNP magnet. Cross section of the NMR cryomagnet with ferroshim tubes integrated in the room-temperature bore generating a second homogeneous field region of 0.32 T (upper position of the NMR/DNP sample) 468 mm above the main magnetic field center of 14 T (lower position of the NMR/DNP sample).

Figure 4: **Schematic of the sample shuttle DNP spectrometer and experimental timing scheme**. (a) The lower homogeneous fieldspot for high field NMR at 14.1 T, 600 MHz and the upper homogeneous fieldspot for EPR and DNP at 0.34T, 9.6 GHz. The upper homogeneous fieldspot is located in the strayfield of the NMR cryomagnet and the field homogeneity is achieved through tubes made of ferromagnetic alloys (ferroshim tubes) aligned coaxially to the upper part of the magnet bore. (b) Timing diagram for the shuttle spectrometer. The sample first resides in the upper homogeneous spot at low field (0.34 T) where microwave irradiation of the sample and the DNP step takes place. Subsequently the sample is rapidly transferred to the high field position (14 T) in the lower part of the NMR cryomagnet where NMR experiments can be performed.

Figure 5: Microwave resonator for sample shuttle DNP setup. (a) Distribution of the microwave TM_{11} electric and magnetic field in a cross sectional plane orthogonal to the cylindrical X band resonator axis. The magnetic field of the resonator is parallel to the

direction of the main constant magnetic field. The blue-coloured regions represent negative amplitudes, the red-coloured regions positive amplitudes of the fields. (b) Cross-sections drawings of the resonator used for the RMM microwave field simulation.

Figure 6: Schematic Diagram of the Probe-Shuttle DNP/CIDNP Setup Probehead and mechanical transfer unit with stepping motor and toothed belt **(**green); auxiliary electromagnet and compensation coil **(**brown) ; computer for transfer control and NMR spectrometer functions (blue)**;** pulsed laser for optical excitation (orange)**.** Inset at upper left: contour of fringe field (black) and its gradient (red) as function of distance from detection position.

Figure 7: Timing scheme of pulsed DNP with field-cycling. Left diagram (a): experimental field excursion within the DNP experiment. 1: MW excitation, 2: Probe shuttle, 3: NMR detection. Right diagram (b): definition of times of the pulsed MW excitation scheme.

Figure 8: Block Diagram of the DNP setup. PDG: pulse delay generator; PTS: frequency synthesizer; AWG: arbitrary waveform generator; HP: high power amplifier.

Figure 9: High-Field microwave bridge. 1- Mechanical switch; 2- 260 GHz solid-state source; 3- corrugated waveguide; 4, 15, 21, 23- tapers to metal-dielectric waveguide; 5- waveguide adapter; 6, 25- dummy loads; 7, 17- variable attenuator; 8- beam splitter; 9- grid; 10, 12, 13, 19- metal-dielectric waveguides; 11- polarization convertor; 16- double resonance structure; 18- wavemeter; 20- tunable reflector; 22, 24- Schottky detectors.

Figure 10: High frequency helix cylindrical double resonant structure. The helical coil is connected to the RF circuit at 392 MHz for NMR and builds the tube of a cylindrical microwave resonator at 260 GHz for EPR excitation. The microwave magnetic field coupled through a fundamental waveguide and an elliptical iris into the resonator is calculated by a finite element program (ANSOFT v12, U.S.A.).

Figure 11: High-Field DNP results in liquids. 400 MHz water proton signal with (red) and without (black) microwave excitation at 260 GHz. Sample consists of 24 mM TEMPOL in water at room temperature; total sample volume 100 nl. A MW power of 2.6 W was used for the excitation.

Fig 12. X-band DNP setup. The optimized DNP set up at 0.35 T consisting of commercially available EPR and NMR spectrometers with an additional microwave amplifier and an option to observe the cavity dip at high microwave power. Figure from Ref. **[53]**)

Figure 13: DNP power curve at 9.4 T. Shown is the inverse DNP enhancement as a function of the inverse microwave power for Fremy's salt and TEMPOL radical in liquid solution (260 GHz EPR / 400 MHz proton NMR frequency). Figure from Ref. **[62]**.

Figure 14: Proton NMR dispersion curve. ^{1}H water proton relaxation rates of TEMPOL (5 and 10 mM, 298 K) as a function of the applied magnetic field. Figure from Ref. **[52]**.

Figure 15: **DNP coupling factors calculated from the MD simulations**. Shown are results at 25°C from Ref. **[64]**. They decrease approximately as the inverse of the microwave frequency at high frequencies (black line). In contrast, the analytical expressions, most commonly used to rationalize liquid DNP data, drop approximately with $1/B_0^2$ or $1/B_0^{1.5}$ at high frequencies for rotational or translational diffusion respectively, predicting unrealistically small enhancements at high magnetic fields.

Figure16: Coherent effects induced by fast field changes. Dependence of H4 and H7 signal intensities on evolution time, τ_{ev}, at B_{ev} = 0.157T for a) fast field variation (τ_{fv} = 0.29s), stars: H4; open circles: H7, and b) in comparison to slow field variation (τ_{fv} = 1.05s), full triangles: H4; open triangles: H7

Figure 17: NMRD of a system of coupled spins. Relaxation time dispersion of His protons: experimental data (■ - H2, ● - H4, ◆ - α-CH-proton, △ - β_1-CH2-proton, ▽ - β_2-CH2-

proton and ▲ - CH_3-protons) and simulation (line with corresponding color). Relaxation times T_1 are shown instead of rates R_1 to emphasis the specific effects at the nuclear level anti-crossings.

Figure 18: NMRD of lysozyme. Collective protein proton relaxation rates for a 2.8 mM lysozyme solution in D_2O at pH* 3.5 (solid symbols) and for albumin 0.94 mM at pH* 7.4 (open symbols).

Figure 19: Proton DNP for sample shuttle of ethanol. Proton spectrum of ethanol at room temperature (black) vs. the DNP enhanced spectrum (red) of 0.1 M ethanol 80/20 H2O/D2O with 5 mM TEMPONE-D,15N and 10 mM DSS solution. The reference signal was measured with a standard experiment consisting of a short $\pi/2$ pulse with duration of 7.1 µs.

Figure 20: Proton DNP for sample shuttle of glucose. Proton spectrum of glucose at 26.9 °C (black) vs. the DNP enhanced spectrum at 60.3 °C (red) of 0.5 M D – glucose in 99.8% D_2O with 10 mM TEMPONE-D,^{15}N and 5 mM DSS solution. The reference signal was measured with a standard experiment consisting of a short $\pi/2$ pulse with duration of 7.2 µs.

Figure 21: Pulse DNP enhancement ε of 1mM ^{14}N TEMPOL in H_2O. (Left) Variation of DNP amplitude as a function of the duration τ_p of the pump pulse. The numbers given represent the duty cycle. For each curve the product of duty cycle and power amplitude is kept constant. (Right) Dependence of ε at fixed electron magnetization flip angle $\varphi=\pi$ (25 ns) on delay time $\tau=\tau_r-\tau_p$.

Figure 22: Calculated polarization transfer efficiency. Maximum transfer efficiency η for an electron-nuclear two-spin system with hyperfine coupling a = 10 MHz and maximum MW and RF amplitudes of 4 MHz and 20 kHz, respectively. The black and grey lines are the TOP (time-optimal max pulse) curves representing the maximum GRAPE transfer amplitude from

initial electron polarization to transverse (solid circles) and longitudinal (solid squares) nuclear magnetization as a function of transfer time t.

Figure 23: Calculation of proton enhancements for idealized ^{1}H, ^{15}N, hyperfine coupled electron-spin system. Absolute value of the enhancement of proton polarization for an idealized model system consisting of one electron spin, one ^{15}N spin and one proton spin (system B in Ref. **[92]**). The solid curve and solid squares represent the TOP curve of maximal enhancement as a function of pulse sequence duration in the presence of hyperfine couplings. The open squares correspond to optimal enhancement in the absence of hyperfine couplings, i.e. only based on incoherent cross relaxation effects. For comparison, the dotted and dashed curves also show the maximum enhancement of spin I polarization in the model system for saturation and inversion of spin S, respectively.

Figure 24: DNP enhancements of nitroxide radicals in water at different magnetic field values. The experimentally observed enhancements are shown with black circles. The maximum enhancement (assuming s =1 and f =1, predicted from MD calculations for TEMPOL in water (red) and from the force-free model (yellow) are given for temperatures ranging from 25-45°C. The translational and rotational correlation times for the force-free model calculation are taken from NMRD measurements.

Figure 25: NMRD for concavalin A. The water ^{1}H NMRD curve for the metal ion complex Mn^{2+} concanavalin A.

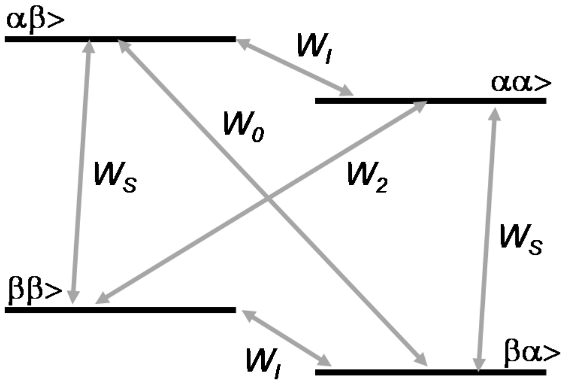

Figure 1

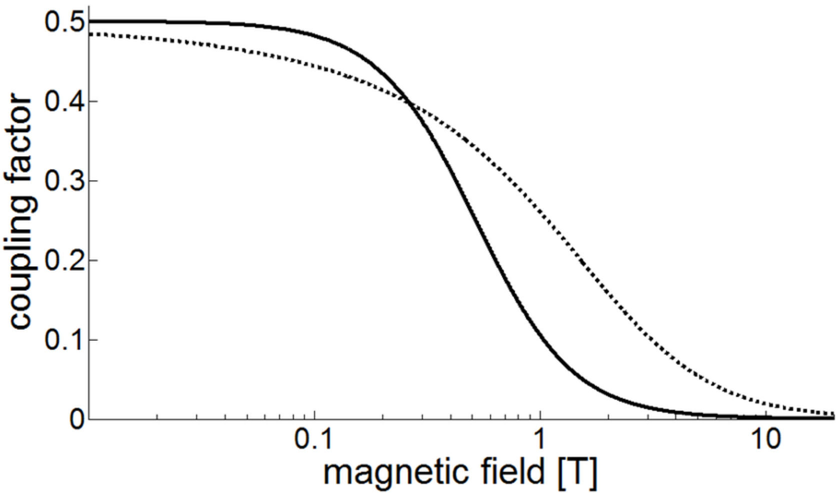

Figure 2

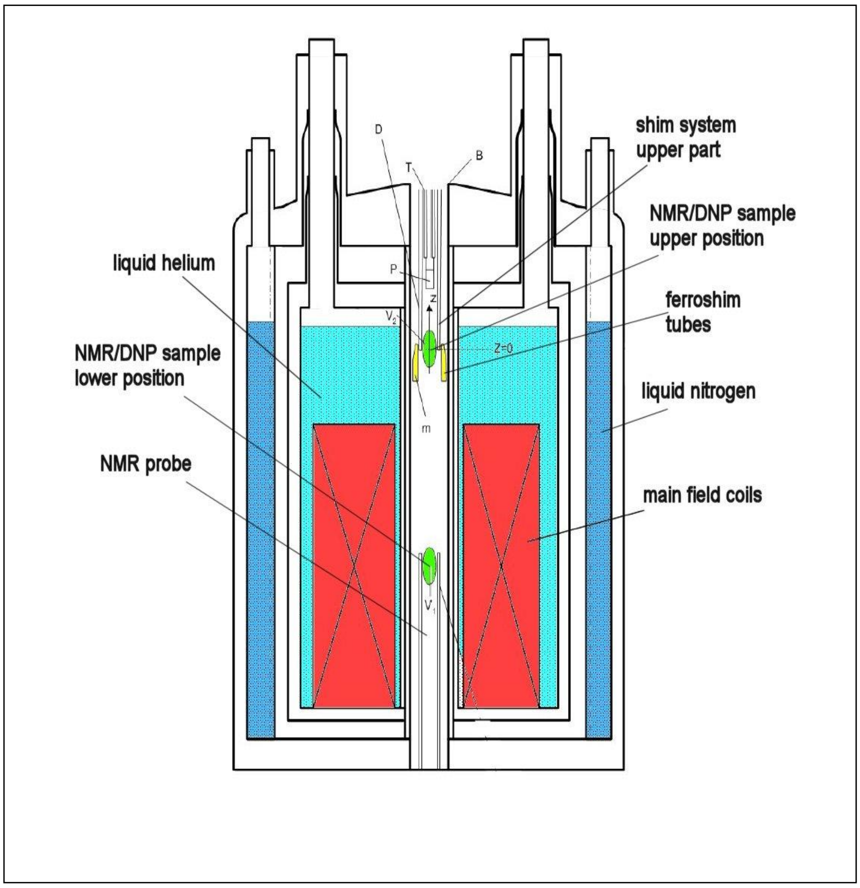
D
T
B
shim system upper part
NMR/DNP sample upper position
liquid helium
P
z
V2
ferroshim tubes
Z=0
NMR/DNP sample lower position
liquid nitrogen
m
NMR probe
main field coils
V1

Figure 3

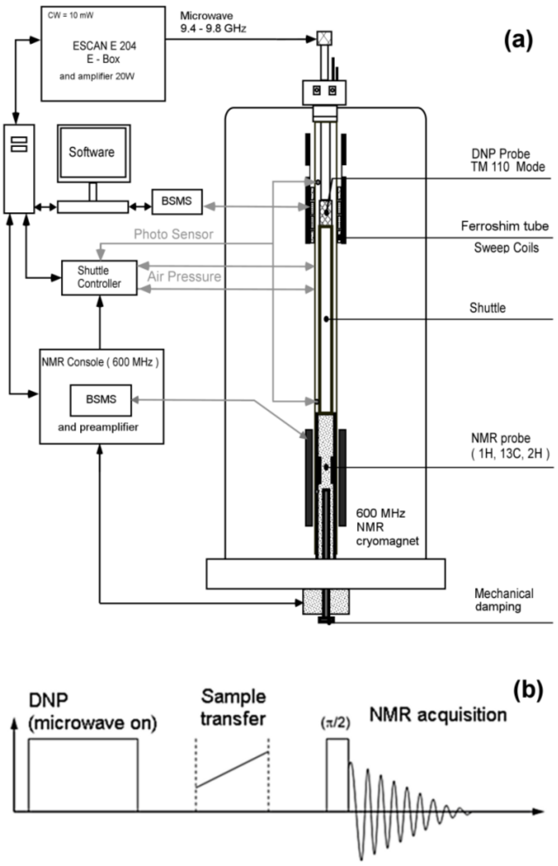
CW = 10 mW
ESCAN E 204
E - Box
and amplifier 20W
Microwave
9.4 - 9.8 GHz
(a)
Software
BSMS
Photo Sensor
Shuttle
Controller
Air Pressure
NMR Console (600 MHz)
BSMS
and preamplifier
DNP Probe
TM 110 Mode
Ferroshim tube
Sweep Coils
Shuttle
NMR probe
(1H, 13C, 2H)
600 MHz
NMR
cryomagnet
Mechanical
damping
(b)
DNP
(microwave on)
Sample
transfer
(π/2)
NMR acquisition

Figure 4

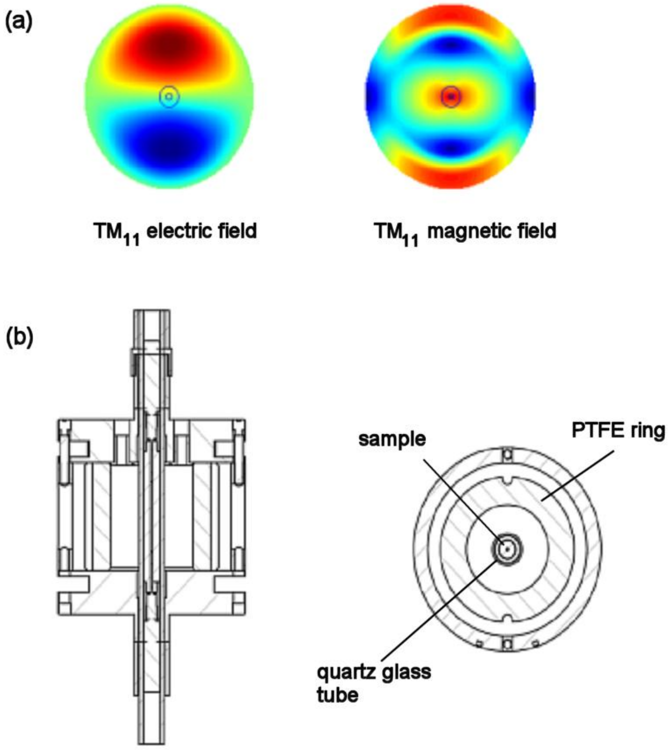
(a)
TM$_{11}$ electric field
TM$_{11}$ magnetic field
(b)
sample
PTFE ring
quartz glass tube

Figure 5

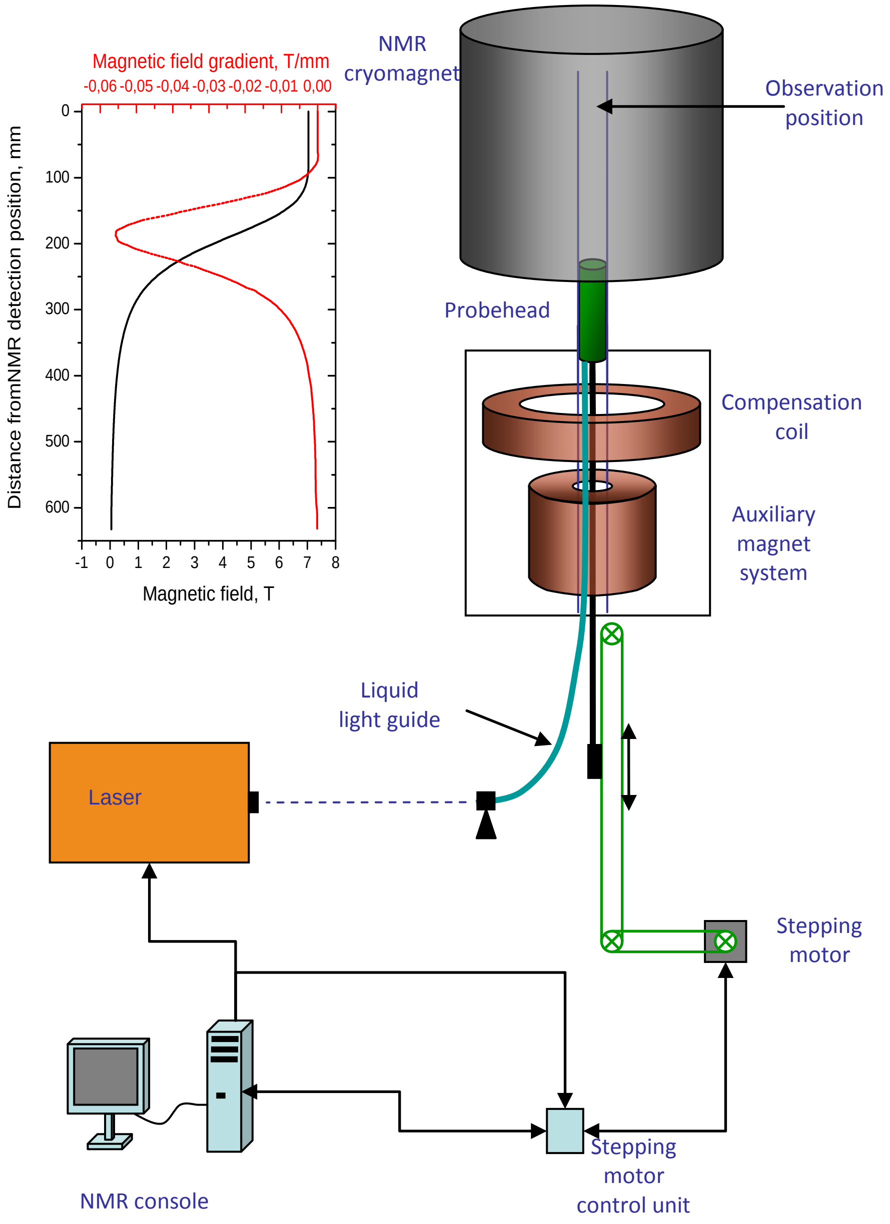
Magnetic field gradient, T/mm
-0,06 -0,05 -0,04 -0,03 -0,02 -0,01 0,00
Distance fromNMR detection position, mm
0
100
200
300
400
500
600
-1 0 1 2 3 4 5 6 7 8
Magnetic field, T
NMR
cryomagnet
Observation
position
Probehead
Compensation
coil
Auxiliary
magnet
system
Liquid
light guide
Laser
Stepping
motor
NMR console
Stepping
motor
control unit

Figure 6

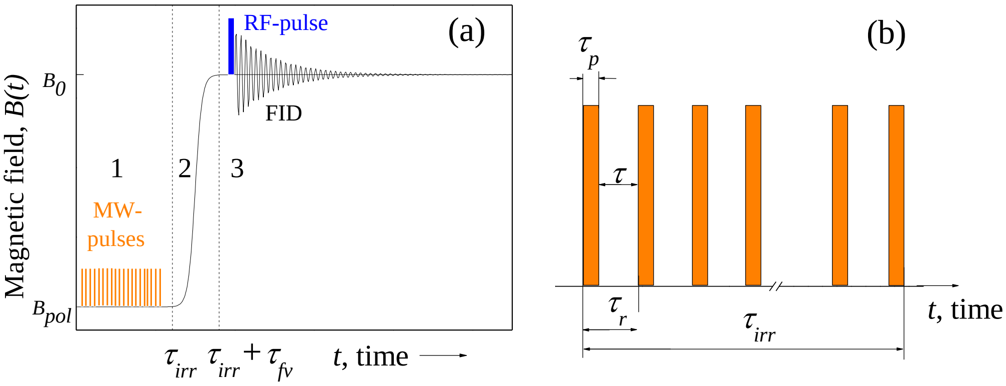
(a)
Magnetic field, B(t)
B_0
B_{pol}
1
2
3
MW-pulses
RF-pulse
FID
τ_{irr}
$\tau_{irr} + \tau_{fv}$
t, time
(b)
τ_p
τ
τ_r
τ_{irr}
t, time

Figure 7

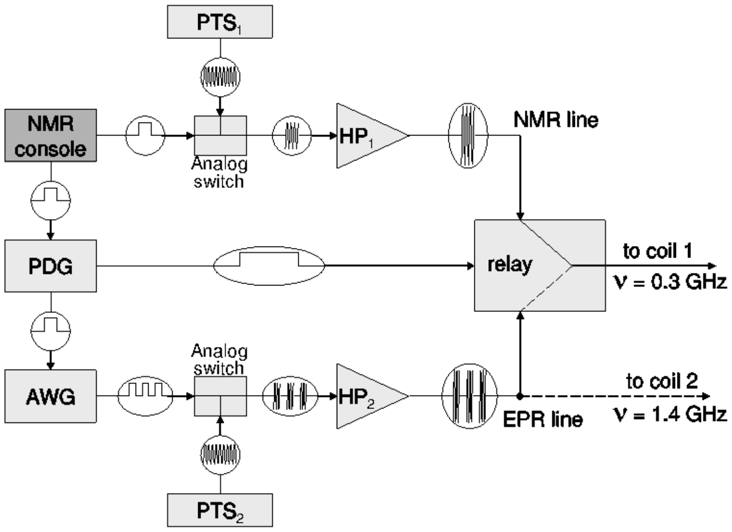
PTS$_1$
NMR console
Analog switch
HP$_1$
NMR line
PDG
relay
to coil 1
ν = 0.3 GHz
AWG
Analog switch
HP$_2$
to coil 2
EPR line
ν = 1.4 GHz
PTS$_2$

Figure 8

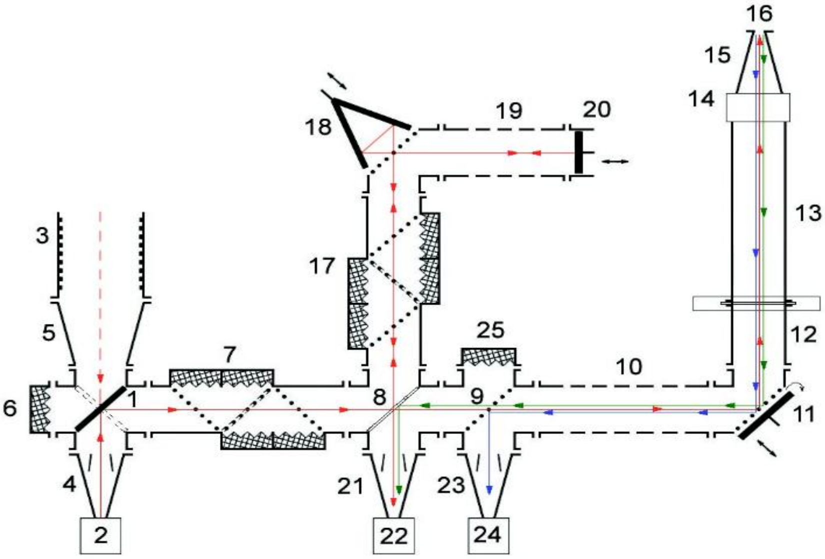

Figure 9

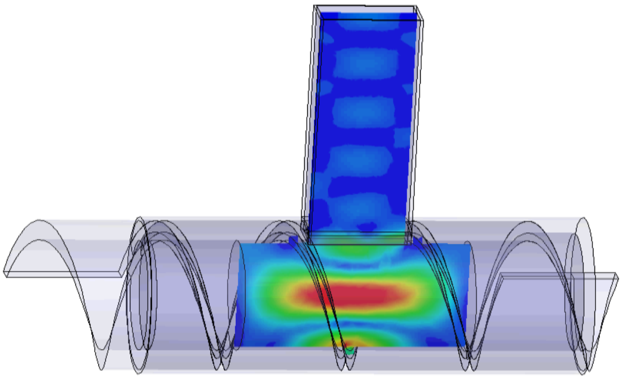

Figure 10

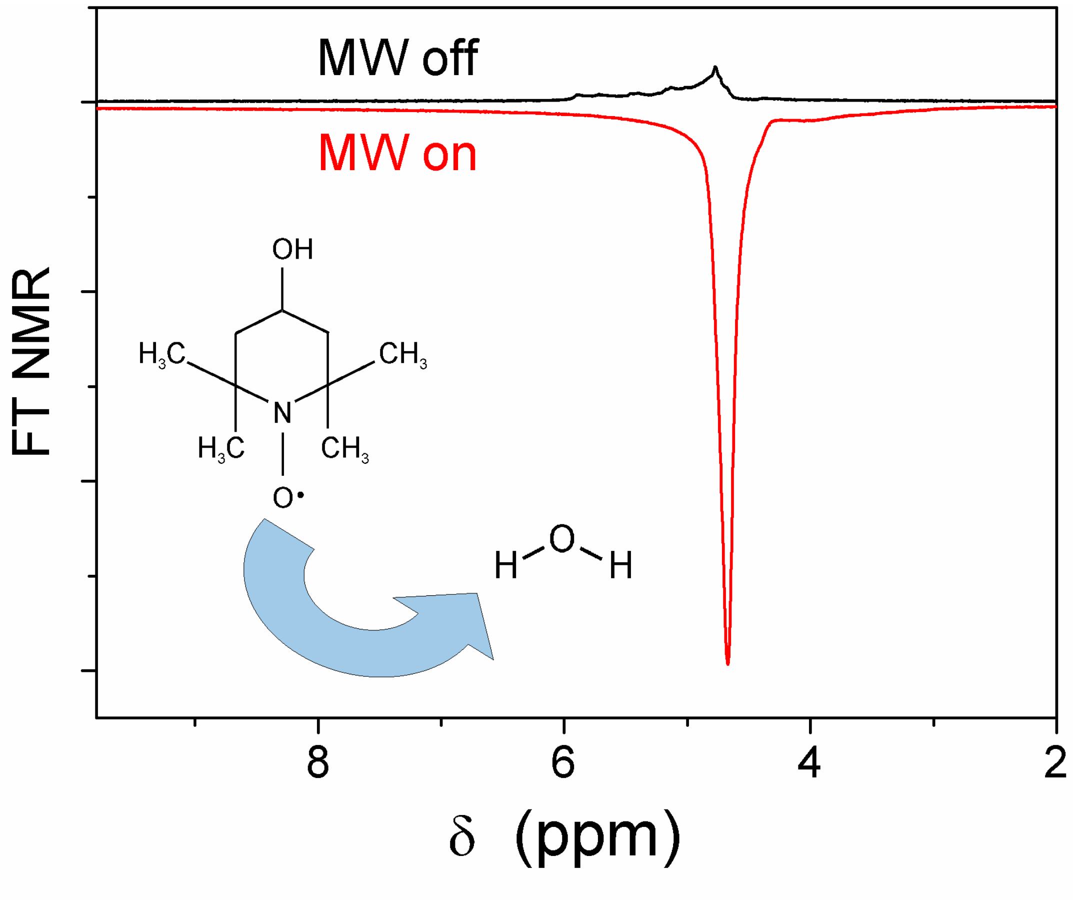

Figure 11

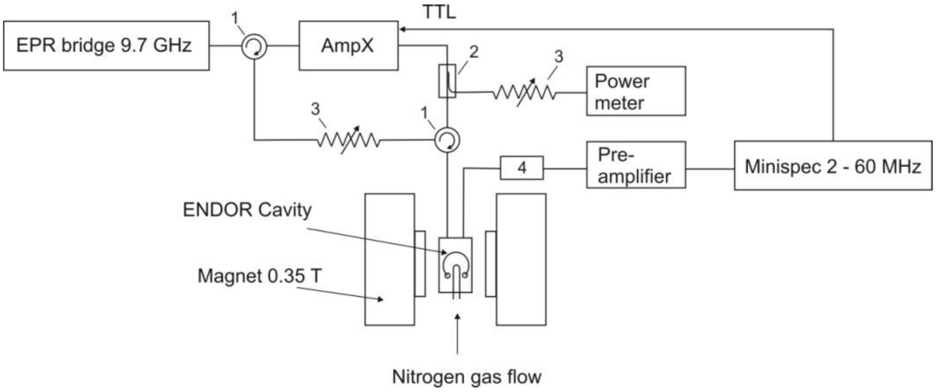
TTL
1
EPR bridge 9.7 GHz
AmpX
2
3
Power meter
3
1
4
Pre-amplifier
Minispec 2 - 60 MHz
ENDOR Cavity
Magnet 0.35 T
Nitrogen gas flow

Figure 12

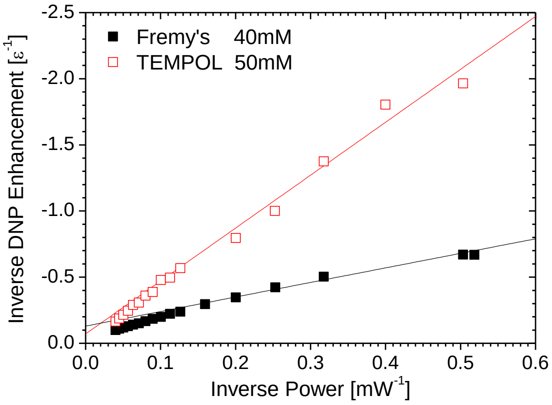
Fremy's 40mM
TEMPOL 50mM
Inverse DNP Enhancement [ε^{-1}]
Inverse Power [mW^{-1}]
-2.5
-2.0
-1.5
-1.0
-0.5
0.0
0.0
0.1
0.2
0.3
0.4
0.5
0.6

Figure 13

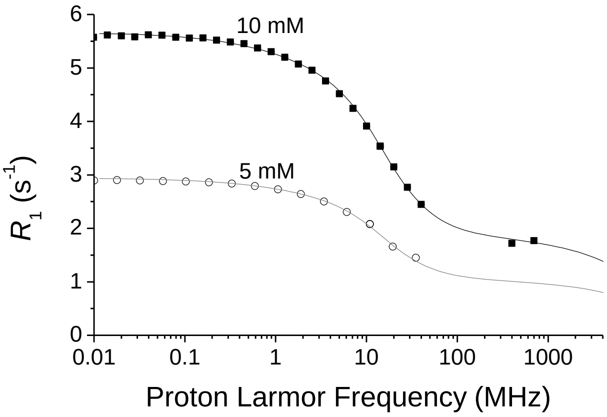
10 mM
5 mM
R_1 (s^{-1})
0
1
2
3
4
5
6
0.01
0.1
1
10
100
1000
Proton Larmor Frequency (MHz)

Figure 14

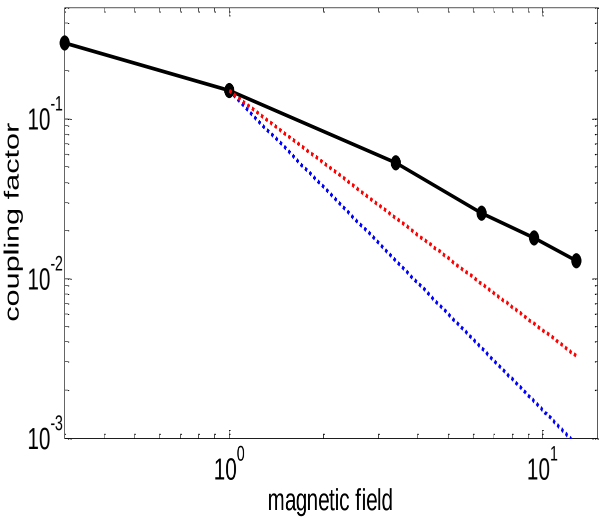

Figure 15

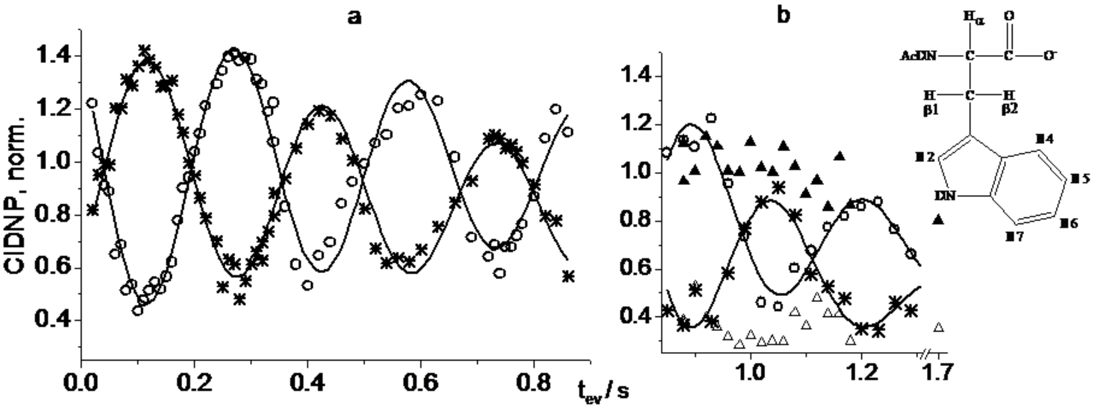
a
b
CIDNP, norm.
1.4
1.2
1.0
0.8
0.6
0.4
0.0
0.2
0.4
0.6
0.8
t$_{ev}$ / s
1.0
1.2
1.7
Hα
O
AcDN
C
O⁻
H
β1
H
β2
H2
H4
H5
H6
H7
DN

Figure 16

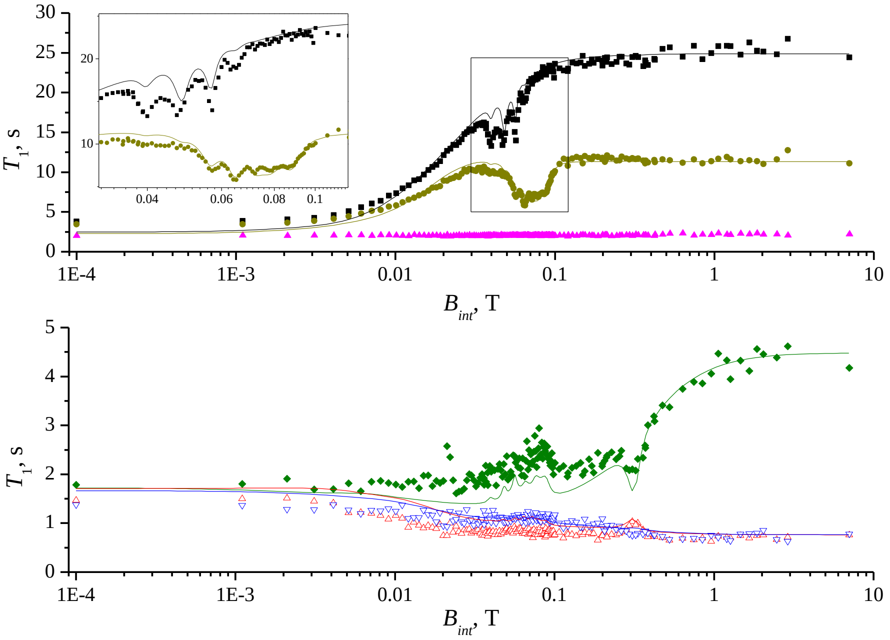
30
25
20
15
10
5
0
T_1, s
20
10
0.04
0.06
0.08
0.1
1E-4
1E-3
0.01
0.1
1
10
B_{int}, T
5
4
3
2
1
0
T_1, s
1E-4
1E-3
0.01
0.1
1
10
B_{int}, T

Figure 17

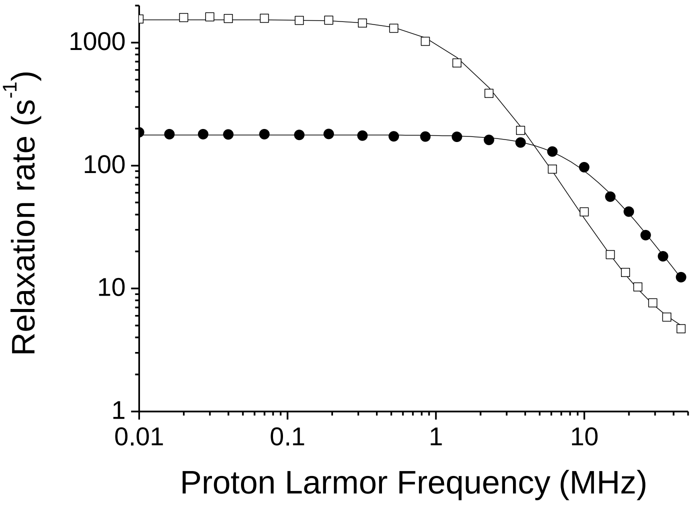
Relaxation rate (s^{-1})
1000
100
10
1
0.01
0.1
1
10
Proton Larmor Frequency (MHz)

Figure 18

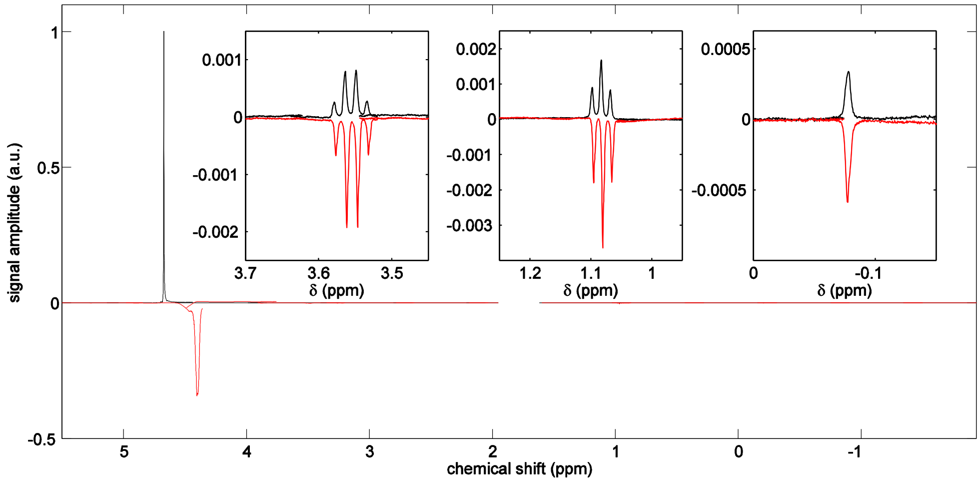
signal amplitude (a.u.)
1
0.5
0
-0.5
5
4
3
2
1
0
-1
chemical shift (ppm)
0.001
0
-0.001
-0.002
3.7
3.6
3.5
δ (ppm)
0.002
0.001
0
-0.001
-0.002
-0.003
1.2
1.1
1
δ (ppm)
0.0005
0
-0.0005
0
-0.1
δ (ppm)

Figure 19

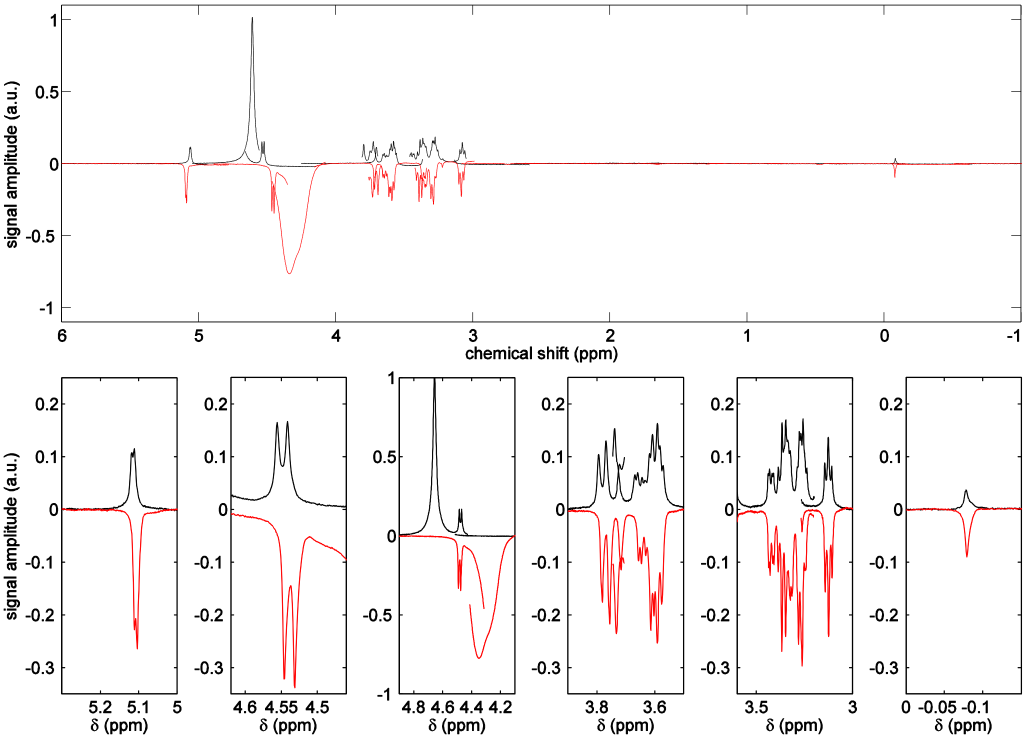
signal amplitude (a.u.)
1
0.5
0
-0.5
-1
6
5
4
3
2
1
0
-1
chemical shift (ppm)
signal amplitude (a.u.)
0.2
0.1
0
-0.1
-0.2
-0.3
5.2
5.1
5
δ (ppm)
4.6
4.55
4.5
δ (ppm)
4.8
4.6
4.4
4.2
δ (ppm)
3.8
3.6
δ (ppm)
3.5
3
δ (ppm)
0
-0.05
-0.1
δ (ppm)

Figure 20

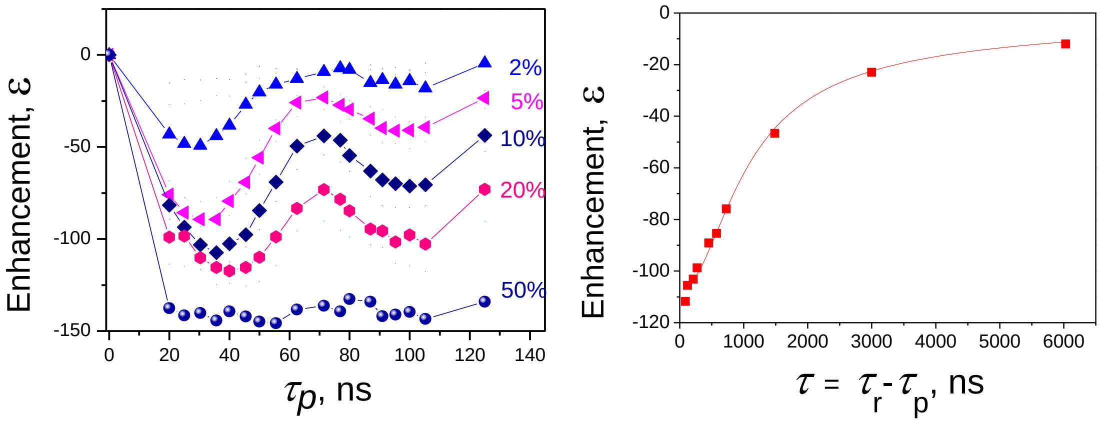
Enhancement, ε
0
-50
-100
-150
0
20
40
60
80
100
120
140
τ_p, ns
2%
5%
10%
20%
50%
Enhancement, ε
0
-20
-40
-60
-80
-100
-120
0
1000
2000
3000
4000
5000
6000
$\tau = \tau_r - \tau_p$, ns

Figure 21

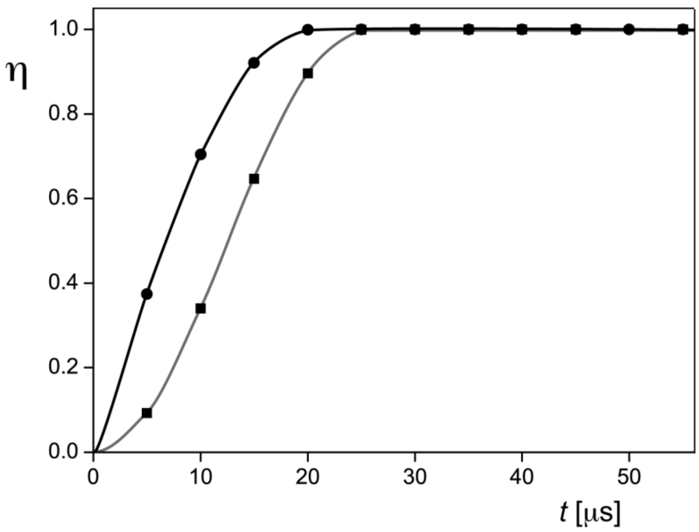

Figure 22

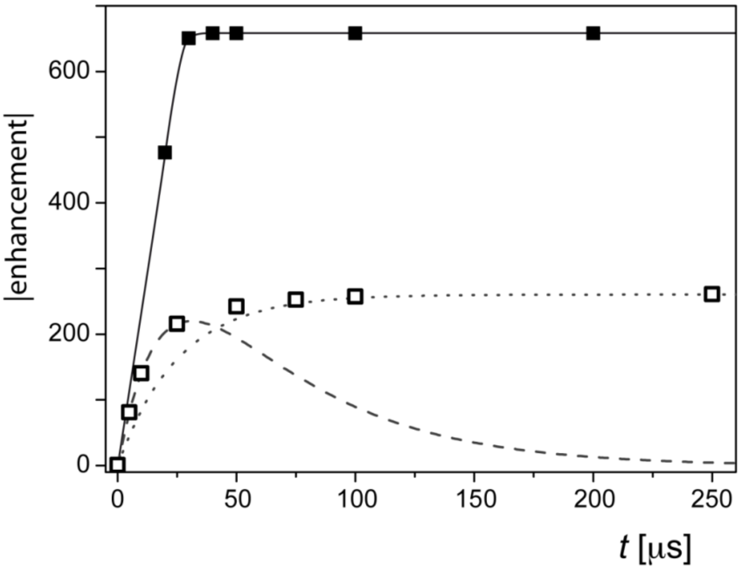

Figure 23

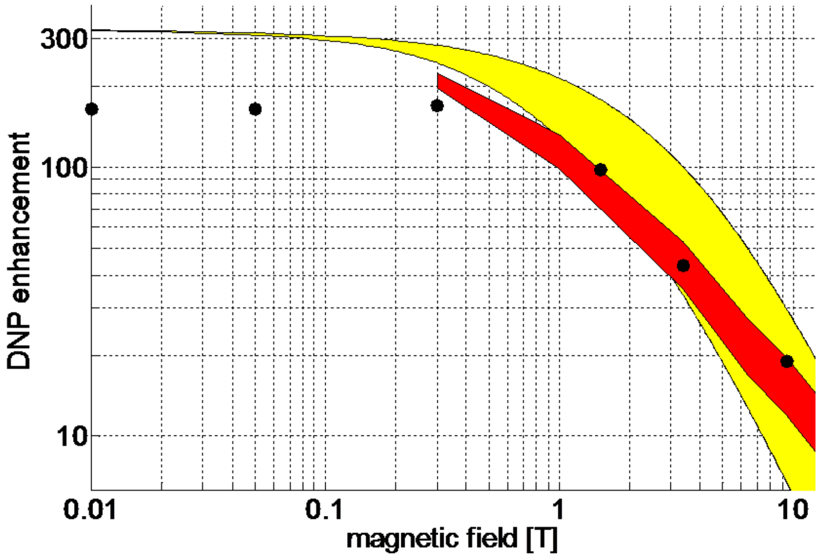

Figure 24

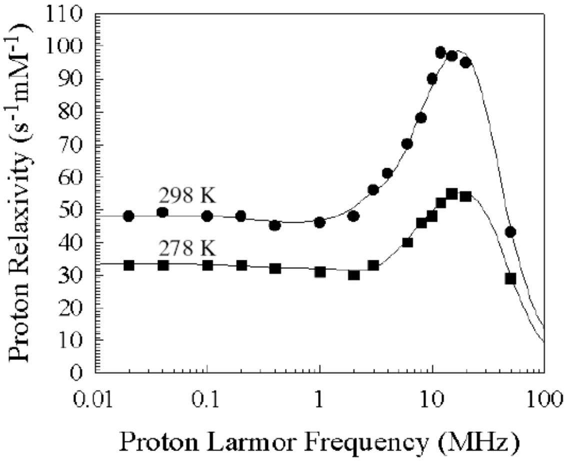
Proton Relaxivity (s^{-1}mM^{-1})
110
100
90
80
70
60
50
40
30
20
10
0
298 K
278 K
0.01
0.1
1
10
100
Proton Larmor Frequency (MHz)

Figure 25